ISPRS Journal of Photogrammetry and Remote Sensing 194 (2022) 1–20

Contents lists available at ScienceDirect

ISPRS Journal of Photogrammetry and Remote Sensing

journal homepage: www.elsevier.com/locate/isprsjprs

Estimating 10-m land surface albedo from Sentinel-2 satellite observations using a direct estimation approach with Google Earth Engine

Xingwen Lin [a], Shengbiao Wu [b,*], Bin Chen [b,c,d], Ziyu Lin [e], Zhengbing Yan [e], Xiuzhi Chen [f], Gaofei Yin [g], Dongqin You [h], Jianguang Wen [h,i], Qiang Liu [j], Qing Xiao [h,i], Qinhuo Liu [h,i], Raffaele Lafortezza [k,l]

[a] College of Geography and Environmental Sciences, Zhejiang Normal University, Jinhua 321004, China
[b] Future Urbanity & Sustainable Environment (FUSE) Lab, Division of Landscape Architecture, Department of Architecture, Faculty of Architecture, The University of Hong Kong, Pokfulam, Hong Kong Special Administrative Region, China
[c] Urban Systems Institute, The University of Hong Kong, Pokfulam, Hong Kong Special Administrative Region, China
[d] Musketeers Foundation Institute of Data Science, The University of Hong Kong, Pokfulam, Hong Kong Special Administrative Region, China
[e] Division for Ecology and Biodiversity, School of Biological Sciences, The University of Hong Kong, Pokfulam, Hong Kong Special Administrative Region, China
[f] Guangdong Province Key Laboratory for Climate Change and Natural Disaster Studies, School of Atmospheric Sciences, Sun Yat-sen University, Zhuhai 519082, China
[g] Faculty of Geosciences and Environmental Engineering, Southwest Jiaotong University, Chengdu 610031, China
[h] Stake Key Laboratory of Remote Sensing Science, Aerospace Information Research Institute, Chinese Academy of Sciences, Beijing 100083, China
[i] University of Chinese Academy of Sciences, Beijing 100049, China
[j] Pengcheng Laboratory, Zhenzhen 518055, China
[k] Department of Agricultural and Environmental Sciences, University of Bari Aldo Moro, Via Amendola 165/A 70126 Bari, Italy
[l] Department of Geography, The University of Hong Kong, Pokfulam, Hong Kong Special Administrative Region, China

ARTICLE INFO

Keywords:
Flux network
High-resolution satellite
Sentinel-2 reflectance
MODIS BRDF/albedo
Spatial heterogeneity
Temporal dynamics

ABSTRACT

Land surface albedo plays an important role in controlling the surface energy budget and regulating the biophysical processes of natural dynamics and anthropogenic activities. Satellite remote sensing is the only practical approach to estimate surface albedo at regional and global scales. It nevertheless remains challenging for current satellites to capture fine-scale albedo variations due to their coarse spatial resolutions from tens to hundreds of meters. The emerging Sentinel-2 satellites, with a high spatial resolution of 10 m and an approximate 5-day revisiting cycle, provide a promising solution to address these observational limitations, yet their potentials remain underexplored. In this study, we integrated the Sentinel-2 observations with an updated direct estimation approach to improve the estimation and monitoring of fine-scale surface albedo. To enable the capability of the direct estimation approach at a 10-m scale, we combined the 10-m resolution European Space Agency (ESA) WorldCover land cover data and the 500-m resolution Moderate-Resolution Imaging Spectroradiometer (MODIS) Bidirectional Reflectance Distribution Function (BRDF)/albedo product to build a high-quality and representative BRDF training database. To evaluate our approach, we proposed an integrated evaluation framework leveraging 3-D physical model simulations, ground measurements, and satellite observations. Specifically, we first simulated a comprehensive dataset of Sentinel-2-like surface reflectance and broadband albedo across a variety of geometric configurations using the MODIS BRDF training samples. With this dataset, we built the Look-Up-Tables (LUTs) that connect surface broadband albedo and Sentinel-2 reflectance through a direct angular bin-based linear regression approach, and further coupled these LUTs with the Google Earth Engine (GEE) cloud-computing platform. We next evaluated the proposed algorithm at two spatial levels: (1) 10-m scale for absolute accuracy assessment using the references from the Discrete Anisotropic Radiative Transfer (DART) simulations and flux-site observations, and (2) 500-m scale for large-scale mapping assessment by comparing the estimated albedo with the MODIS albedo product. Lastly, we presented four examples to show the capability of Sentinel-2 albedo in detecting fine-scale characteristics of vegetation and urban covers. Results show that: (1) the proposed algorithm accurately estimates surface albedo from Sentinel-2-like reflectance across different landscape configurations (overall root-mean-square-error (RMSE) = 0.018, bias = 0.005, and coefficient of

* Corresponding author at: Division of Landscape Architecture, Faculty of Architecture, The University of Hong Kong, Pokfulam, Hong Kong Special Administrative Region, China.
E-mail address: shengwu@hku.hk (S. Wu).

https://doi.org/10.1016/j.isprsjprs.2022.09.016
Received 7 May 2022; Received in revised form 25 July 2022; Accepted 23 September 2022
Available online 14 October 2022

determination (R^2) = 0.88); (2) the Sentinel-2-derived surface albedo agrees well with ground measurements (overall RMSE = 0.030, bias = -0.004, and R^2 = 0.94) and MODIS products (overall RMSE = 0.030, bias = 0.021, and R^2 = 0.97); and (3) Sentinel-2-derived albedo accurately captures seasonal leaf phenology and rapid snow events, and detects the interspecific (or interclass) variations of tree species and colored urban rooftops. These results demonstrate the capability of the proposed approach to map high-resolution surface albedo from Sentinel-2 satellites over large spatial and temporal contexts, suggesting the potential of using such fine-scale datasets to improve our understanding of albedo-related biophysical processes in the coupled human-environment system.

1. Introduction

Land surface albedo—the fraction of radiative flux reflected by a surface to the atmosphere —is a critical variable in estimating the global surface energy budget (Dickinson, 1983; Liang et al. 2019; Schaaf et al. 2002). It is one of the essential climate variables that reflect the variations, patterns, and drivers of the Earth's climate by regulating the biophysical effects of natural events or human activities (Shuai et al. 2014; Zeng et al. 2021). It is also tightly connected with several biogeochemical and hydrological cycles as the absorbed radiant flux (e.g. absorbed photosynthetically active radiation) drives the processes of plant photosynthesis, vegetation growth, and evapotranspiration (Chen and Liu, 2020; Marshall et al. 2018; Zhang et al. 2020a). Therefore, an accurate estimation of land surface albedo helps quantify the global surface energy budget and understand the biogeochemical and hydrological processes for improving predictions of future climate change within the context of increasing anthropogenic impacts.

Increasing interest has particularly focused on the accurate mapping of fine-scale surface albedo, especially for the spatial resolution varying from a few to tens of meters (Li et al. 2018; Shuai et al. 2014). Fine-scale land surface presents spatially detailed characteristics of the landscape. Thus, the fine-scale variability in surface albedo reflects multiple relevant local- and landscape-scale biophysical processes of natural events and anthropogenic activities, including the land surface energy budget and radiative forcing, canopy photosynthesis and transpiration, wildfire burning, snowfall and snowmelt, urban expansion, and heat island effect (Baldinelli et al. 2015; Hu et al. 1999; Mihailovic et al. 2012; Potter et al. 2020; Schwerdtfeger, 2002; Trlica et al. 2017; Wang and Davidson, 2007). An increasing number of recent studies have proven the great potential of fine-scale surface albedo for many other practical applications, such as forestry management (Kuusinen et al. 2014; Vanderhoof et al. 2014), agricultural monitoring (Gao et al. 2014; Li and Fang, 2015), and accuracy assessments of satellite products (Lin et al. 2018; Román et al. 2013; Wu et al. 2016). Therefore, an improved estimation and monitoring of fine-scale surface albedo are essential for understanding multiple albedo-driven biophysical processes and facilitating albedo-related practical applications.

Multi-source remote sensing approaches have paved the way for monitoring surface albedo across different spatial and temporal scales. Tower-based flux network is the most accurate way to record surface albedo but is constrained to the local spatial extent with an effective footprint of several hundred to thousands of meters (Baldocchi et al. 2001; Cescatti et al. 2012; Chu et al. 2021). Drone flights are an alternative to flux-site observations for quantifying surface albedo with broader spatial coverage in a cost-effective way, but this approach is also restricted to a limited spatial extent of several hectares (Cao et al. 2018; Levy et al. 2018). Satellite remote sensing is widely recognized as the only practical method for mapping surface albedo at regional and global scales owing to its global spatial coverage and short revisiting cycle (Liang et al. 2013; Schaaf et al. 2002). With the rapidly increasing satellite launches over the past few decades, a variety of global-scale surface albedo products have become available across different spatial and temporal resolutions, such as the Advanced Very High Resolution Radiometer (AVHRR, 5-km spatial resolution and daily temporal resolution; Csiszar and Gutman, 1999), POLarization and Directionality of the Earth's Reflectances (POLDER, 6-km spatial resolution and 10-day temporal resolution; Breon and Maignan, 2017), Multi-angle Imaging SpectroRadiometer (MISR, 1.1-km spatial resolution and 9-day temporal resolution; Diner et al. 1998), Moderate-Resolution Imaging Spectroradiometer (MODIS, 500-m spatial resolution and daily temporal resolution; Schaaf et al. 2002), Global LAnd Surface Satellite (GLASS, 1-km spatial resolution and 8-day temporal resolution; Liang et al. 2013), and Visible Infrared Imaging Radiometer Suite (VIIRS, 500-m spatial resolution and daily temporal resolution; Wang et al. 2013). However, these global products are limited to coarse spatial resolutions that cannot accurately capture the fine-scale dynamics of surface albedo caused by natural (Wang et al. 2016b) and anthropogenic disturbances (Trlica et al. 2017).

High-resolution satellites, especially Sentinel-2 with a 10-m spatial resolution and Landsat with a 30-m spatial resolution, offer an essential alternative to address the observational limitations of traditional coarse-resolution satellite sensors. However, insufficient multi-angular observations preclude using physical BRDF models to directly retrieve surface albedo from high-resolution satellites. Several recent studies have demonstrated the feasibility of fusing such high-resolution satellite reflectance data with traditional coarse-resolution satellite BRDF product to monitor fine-scale surface albedo. For example, Shuai et al. (2011) proposed a MODIS-concurrent approach by integrating the pairs of Landsat surface reflectance and MODIS Bidirectional Reflectance Distribution Function (BRDF)/albedo data to estimate surface albedo with a 30-m spatial resolution. Li et al. (2018) recently extended this approach to the Sentinel-2 satellite to generate surface albedo with a 20-m spatial resolution. These studies have two model assumptions/requirements: (1) an equal ratio of reflectance and albedo between the high-resolution satellites (i.e. Landsat and Sentinel-2) and MODIS with the same land cover; and (2) high-quality MODIS data that is concurrent with the high-resolution satellite for providing BRDF parameters across different land cover types. The major limitation of this type of approach is the lack of real-time high-resolution land cover classification maps, which constrains the practicability of mapping surface albedo over large spatial areas.

Alternatively, the direct estimation approach provides another opportunity to map surface albedo from top-of-atmosphere or surface reflectance by using the pre-built relationships between surface albedo and reflectance (Liang et al. 1999). This approach avoids the real-time data processing of reflectance anisotropy modeling, spectral albedo calculation, and narrowband-to-broadband albedo conversion. He et al. (2018) used this approach to estimate surface albedo from the 30-m Landsat satellites. Zhang et al. (2020b) independently proposed a similar albedo estimation framework with additional prior information of flux-tower measurements. These studies collectively suggest the great potential of using the direct estimation approach for mapping fine-scale surface albedo. However, due to the lack of high-quality BRDF training samples and reliable evaluation datasets at a 10-m scale, the application of this approach remains challenging for the Sentinel-2 satellites with much higher spatial and temporal resolutions but fewer spectral bands (only four 10-m resolution spectral bands). Additionally, previous studies have successfully applied the direct estimation approach to alternative satellites (e.g. Landsat) across individual sites, while the practice of mapping fine-scale surface albedo from the Sentinel-2 satellites over regional and global scales remains a difficult task due to limited computation capability.

The main goal of this study is to develop a direct estimation approach that allows the mapping of fine-scale surface albedo from 10-m Sentinel-2 satellites. It is further divided into three sub-objectives: (1) building a 10-m scale high-quality and representative dataset of BRDF samples for algorithm training and developing a comprehensive albedo evaluation framework; (2) providing a feasible strategy for large-scale albedo mapping; and (3) exploring the practical implications of Sentinel-2 fine-scale albedo. To this end, we first integrated the 10-m resolution European Space Agency (ESA) land cover data and 500-m resolution MODIS BRDF/albedo product to create representative BRDF training samples. We then simulated the pairs of surface albedo and Sentinel-2-like surface reflectance under different illumination and viewing geometry conditions using MODIS BRDF training samples, generated Look-Up-Tables (LUTs) that connect these two quantities, and finally fused these LUTs with the Google Earth Engine (GEE) cloud-computing platform. With this algorithm, we estimated surface albedo from Sentinel-2 and validated the derived albedo with references from 3-D Discrete Anisotropic Radiative Transfer (DART) simulations, tower-mounted flux measurements, and MODIS satellite albedo products. Lastly, we investigated the practical applications of the Sentinel-2 albedo in detecting the fine-scale characteristics of vegetation cover and urban areas.

2. Materials

Two kinds of datasets were used in this study and described in detail as follows.

2.1. Training and calibration datasets

2.1.1. MODIS collection 6 BRDF/albedo product

The 21-year (2000–2020) MCD43A1 and MCD43A3 products with 500-m spatial resolution were used. The MCD43A1 product provides three weighting parameters (isotropic, volumetric, and geometric) for seven narrow bands and three broad bands, allowing to simulate surface reflectance at specific illumination and viewing geometry. The MCD43A3 product offers daily narrowband and broadband albedo for both direct (black-sky albedo, BSA) and diffuse (white-sky albedo, WSA) illumination conditions. The MODIS BRDF/albedo product is accessible at https://modis.gsfc.nasa.gov/data/dataprod/mod43.php. In this study, we downloaded and used MODIS BRDF/albedo for two distinct purposes. First, the MCD43A1 BRDF product of individual samples was used to generate the simulated datasets of broadband albedo and Sentinel-2-like spectral surface reflectance for building the reflectance-to-albedo LUTs using an angular bin-based linear regression (He et al. 2018; Qu et al. 2014; Wang et al. 2015). Second, the MCD43A3 albedo data was selected as the benchmark to assess the accuracy of Sentinel-2-derived surface albedo across regional and global scales.

To collect reliable and representative BRDF data of individual samples, we filtered and downloaded the MODIS observations following four criteria: (1) high quality—using the quality assurance (QA) layer to extract high-quality MODIS pixels (i.e. quality bit index = 0); (2) homogenous coverage—screening out the candidate MODIS pixels along with the surrounding area of 3 × 3 pixels have remained as unchanged land cover (indicated by the MCD12Q1 land cover product) during the last 21 years (2000–2020) and retaining only those pure pixels with a 95 % land cover purity (i.e. the pixel-scale fraction of dominant land cover indicated by the 10-m resolution ESA WorldCover data); (3) variety of land cover—selecting MODIS data across 16 land cover types, except for water body, based on the International Geosphere-Biosphere Programme (IGBP) classification scheme; and (4) reasonable data range—ensuring that the pair values of spectral surface reflectance and albedo calculated from the MCD43A1 BRDF kernel parameters were within the physical range of [0, 1]. According to our sensitivity analysis regarding the impacts of BRDF training samples on algorithm accuracy (see Section 3.1.2 below), a total of 7200 individual MODIS samples with 450 samples for each land cover type were finally selected and used (Fig. 1).

To assess the accuracy of the proposed algorithm over a regional scale, we also downloaded and used the gridded tiles of MCD43A3 albedo products across 16 land cover types with a global area coverage (i.e. sites #a – #p in Fig. 2) during the four seasons of spring, summer, fall, and winter (i.e. one gridded tile per land cover per season) in 2019 (see Section 3.3 below). Each MCD43A3 gridded tile included one dominant land cover type (i.e. fraction of dominant land cover within the grid tile indicated by the 500-m MCD12Q1 product ≥ 50 %) and was quality controlled using the QA layer (i.e. quality bit index = 0).

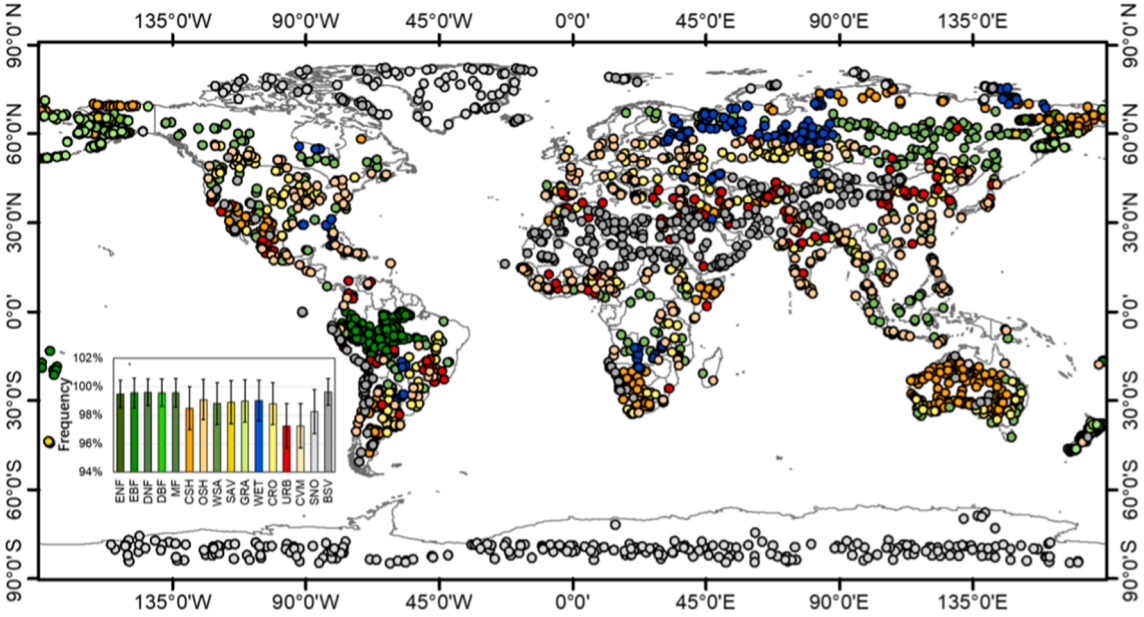

Fig. 1. Geographical distribution of training and testing samples of Moderate Resolution Imaging Spectroradiometer (MODIS) Bidirectional Reflectance Distribution Function (BRDF)/albedo data across 16 land cover types of the International Geosphere-Biosphere Programme (IGBP) classification except for water body. A total of 7200 MODIS BRDF/albedo samples are used, including 400 training and 50 testing samples for each land cover. The inserted figure shows the frequency of land cover homogeneity of 500-m resolution MODIS BRDF training samples that characterized by the 10-m resolution European Space Agency (ESA) land cover mapping data.

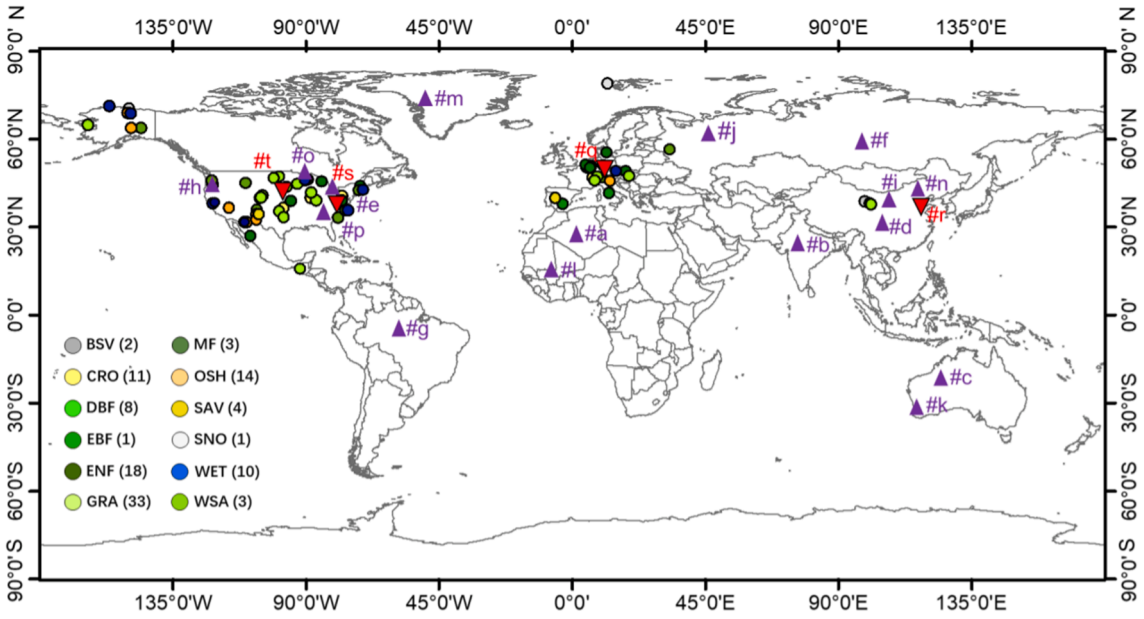

Fig. 2. Geographic distribution of flux sites and gridded tiles for validating Sentinel-2-derived albedos across different land cover types based on the International Geosphere-Biosphere Programme (IGBP) classification, including barren sparse vegetation (BSV), cropland (CRO), deciduous broadleaf forest (DBF), evergreen broadleaf forest (EBF), evergreen needleleaf forest (ENF), grassland (GRA), mixed forest (MF), open shrubland (OSH), savanna (SAV), snow and ice (SNO), wetland (WET), and woody savanna (WSA). Flux sites are indicated by colored circles and the site numbers for each land cover type are shown in parentheses; gridded tiles are indicated by purple triangles labelled with the tile IDs from #a - #p; red triangles with the tile IDs from #q - #t represent four examples showing the practical applications of the Sentienl-2 albedo. (For interpretation of the references to color in this figure legend, the reader is referred to the web version of this article.)

2.1.2. Sentinel-2 surface reflectance product

The Sentinel-2 constellations with two identical polar-orbiting satellites (Sentinel-2A and Sentinel-2B) were launched by the ESA in 2015 and 2017 with the aim of providing high-resolution observations to support the monitoring of the Earth's surface dynamics (Drusch et al. 2012). Both are equipped with the multi-spectral instrument to help collect optical imagery with global coverage from 56°S to 84°N in a wide swath width of 290 km and a frequent revisit cycle of ~ 5 days at the equator. The Sentinel-2 satellite has 13 spectral bands spanning from visible and near-infrared (NIR) to shortwave infrared (SWIR) at different spatial resolutions ranging from 10 to 60 m on the ground with distinct purposes. Specifically, three visible (blue, green, red) and NIR bands at 10-m resolution were designed to ensure continuity mission with the other high-resolution satellites (e.g. Landsat-8) to improve the land cover classification. Six infrared bands (i.e. four red edges, one SWIR-1, and one SWIR-2) at 20-m spatial resolution are used to enhance land-cover classification and improve the retrieval of geophysical parameters. The other three spectral bands at 60 m are dedicated mainly for atmospheric corrections and cirrus-cloud screening (Drusch et al. 2012; Li et al. 2018). Moreover, the high-quality radiometric performance of the Sentinel-2 satellite with a 12-bit radiometric resolution and 5 % radiometric error allowance enables the feasible acquisition of surface signals without saturation (Sentinel-2 Team, 2021). Thus, the high spatial resolution, frequent revisits, wide swath, multispectral features, and high radiometric quality of Sentinel-2 enable the global monitoring of surface dynamics.

The 10-m resolution Level-2A Sentinel-2 surface reflectance products of three visible bands (blue, green, and red) and one NIR spectral band were used in this study and are freely accessed from the GEE platform at https://developers.google.com/earth-engine/datasets/catalog/COPERNICUS_S2_SR. To test the proposed algorithm, we used the three-year (2018–2020) Sentinel-2 surface reflectance data and associated cloud probability product together with default cloud masking parameters (https://developers.google.com/earth-engine/tutorials/community/sentinel-2-s2cloudless). In the main text, we primarily focused on 2019 Sentinel-2 data, with the results of 2018 and 2020 shown in the supplementary materials. The overall results were comparable with those shown for 2019. We used Sentinel-2 data to estimate fine-scale surface albedo, which was validated against ground measurements and MODIS satellite product (see Section 3.2 below) and further evaluated for practical applications (see Section 3.3 below).

2.1.3. Land cover product

To facilitate the selection of pure-pixel BRDF training samples, we used two types of land cover products, including the 10-m resolution ESA WorldCover mapping data in 2020 and the 21-year (2000–2020) 500-m resolution MCD12Q1 land cover product. These two datasets were both downloaded from the GEE platform and used with quality control from the default QA layer.

The MCD12Q1 product was used for two purposes: (1) to help select high-quality MODIS training BRDF samples; and (2) to assess the accuracy and uncertainty of the proposed algorithm over a regional scale. The ESA WorldCover data were used to finalize the 10-m representative BRDF samples from the candidate MODIS pixels based on the above selection of high-quality MODIS training BRDF samples.

2.2. Validation datasets

2.2.1. Tower flux network observations

The measurements of downward and upward solar radiation from five tower flux networks in the 2018–2020 time period were used. These flux networks include four which are globally distributed: Baseline Surface Radiation Network (BSRN), Surface Radiation (SURFRAD), AmeriFlux, European Fluxes Database (EuroFlux), and one regionally distributed Heihe Watershed Allied Telemetry Experimental Research (HiWATER) wireless sensor network (HiWaterWSN). The details of each flux network are provided as follows.

BSRN: managed by the World Radiation Monitoring Center (WRMC) with the aim of providing high-quality observations of shortwave and longwave surface radiation fluxes, together with meteorological and other supportive measurements for validating and evaluating satellite-based estimates of surface radiative fluxes since 1992. This network

measures downward and upward shortwave radiation with direct and diffuse components at 1-min sampling time intervals. The flux datasets are available at https://dataportals.pangaea.de/bsrn/.

SURFRAD: part of BSRN and supported by the National Oceanic and Atmospheric Administration (NOAA) office of global programs with the primary objective of collecting accurate, continuous, and long-term measurements of surface radiation budget over the United States for supporting climate-related research since 1995. This network measures downward and upward shortwave radiation with total, direct, and diffuse components at 1-min recording time intervals through the broadband pyranometers mounted on 10-m flux towers. The SURFRAD network data contained in the BSRN network has been excluded to avoid any duplications. The flux datasets are available at http://www.esrl.noaa.gov/gmd/grad/surfrad/.

AmeriFlux: launched in 1996 and has become one of the most highly regarded networks in climate and ecological research, focusing on climate-relevant responses and terrestrial ecosystem processes. It is now supported by the AmeriFlux Management Project (AMP) of Lawrence Berkeley National Laboratory (LBNL), and offers 30-min observations of downward and upward shortwave solar radiation together with tower height and other meteorological variables. The flux datasets are available at https://ameriflux.lbl.gov/.

EuroFlux: mainly funded by the European Union since 1996 and jointly supported by several research projects (i.e. CarboAfrica, CarboExtreme, GHG-Europe, ICOS, and InGOS) with the primary objective of providing standard and high-quality observations to enhance the understanding of the carbon and water cycles of terrestrial ecosystems. The European network currently manages over 400 flux sites and records downward and upward shortwave radiation at a sampling interval of 30 min, with flux data available at http://www.europe-fluxdata.eu/.

HiWaterWSN: launched during the HiWATER campaign that was conducted over the Chinese Hehei river basin in 2012 with the scientific goal of collecting integrated, distributed, and multi-scale observations to improve the understanding of hydrological processes and ecosystem functioning of arid and semi-arid regions. A wireless sensor network (WSN) with 40 nodes was installed across seven meteorological stations to measure upward and downward shortwave radiation with a 10-min sampling interval (Che et al. 2019). The datasets are freely available from the National Tibetan Plateau/Third Pole Environment Data Center at https://data.tpdc.ac.cn/en/special/heihe/.

Tower height is the key parameter for the effective footprint of flux sites (Román et al. 2013). We thus formulated the flux sites that did not provide auxiliary information of tower height based on two assumptions: (1) for the high-tower flux sites (e.g. forest), we assumed that the flux cameras could be installed at 3 m above the tops of vegetation canopy (Rojas-Robles et al. 2020) and extracted vegetation height from the Global Ecosystem Dynamics Investigation (GEDI) database (Dubayah et al. 2020); and (2) for the low-tower flux sites (e.g. grassland and shrubland), we assumed that flux cameras could be installed at a standard 10-m height similar to the SURFRAD network. To address the impacts of the footprint mismatch between Sentinel-2 spatial resolution and the flux tower footprint, we first assessed the representativeness of available flux sites using two Sentinel-2 albedo images with the coefficient of variation (CV) metric across two leaf development and leaf senescence stages at each site, and then selected those homogeneous sites with a CV less than 10 % as validation sites. A total of 108 flux sites (with 91 site-years in 2018, 97 site-years in 2019, and 68 site-years in 2020) across different land cover types were downloaded and used, including 5 sites from BSRN, 4 sites from SURFRAD, 76 sites from AmeriFlux, 19 sites from EuroFlux, and 4 sites from HiWaterWSN (Fig. 2 and Table 1). In this study, the flux observations were first used to calculate site-level surface albedo, and then as ground truth to validate surface albedo derived from the Sentinel-2 satellites (see Section 3.2 below).

2.2.2. 3-D DART simulations

3-D DART simulations of different landscape configurations were used. With the DART model (Gastellu-Etchegorry et al. 2015), we first created eight sets of 100-m × 100-m archetype scenarios with a 10-m spatial resolution (Fig. 3), covering one homogenous grassland, three-category (i.e. sparse, medium, and dense) heterogeneous forests, two types of built-ups (i.e. one unevenly distributed and one uniformly distributed), and two types of topography (i.e. one sloping surface with solo slope gradient and one rugged terrain that composited with a variety of individual sloping surfaces). We then generated a variety of synthetic scenarios from the archetype scenarios by setting different configurations of canopy structures (indicated by leaf area index (LAI)), solar-viewing geometry, and illumination radiation conditions). These configuration settings include LAI ranging from 1 to 7 with an interval of 2, solar zenith angle ranging from 0° to 60° with an interval of 10°, viewing zenith angle ranging from 0° to 20° with an interval of 10°, relative azimuth angle ranging from 0° to 180° with an interval of 45°, and two diffuse skylight ratios of 0 and 1. We specifically built a set of sloping surfaces (Fig. 3g) with the slope gradient ranging from 0° to 60° with an interval of 10° and the aspect gradient ranging from 0° to 180° with an interval of 45°. A total of 35, 280 scenarios were generated, covering all possible combinations of configuration parameters. With the typical leaf (deciduous leaf), ground (brown sandy loam), building (red cement), and road (gray concrete) properties, we finally simulated synthetic images of surface hyperspectral reflectance and albedo across different landscape configurations, and generated a synthetic dataset of Sentinel-2-like surface reflectance and shortwave albedo by spectral integration with the prior information of the relative spectral response (RSR) function profiles of Sentinel-2.

3. Methodology

We divided the methodology into the following three major steps: (1) building the direct estimation approach of angular bin-based regression using the simulated datasets of surface reflectance and albedo; (2) validating the proposed algorithm with references from the 3-D DART simulations, ground-based measurements, and MODIS albedo product; and (3) exploring the practical applications of Sentinel-2-derived albedo in detecting fine-scale surface characteristics. A flowchart that summarizes these major steps is shown in Fig. 4.

3.1. Developing the direct estimation approach

We divided this task into the following two sub-steps.

3.1.1. Generating simulated datasets of surface reflectance and albedo from MODIS data

The MODIS BRDF data of individual samples across different land cover types were primarily used to simulate datasets of Sentinel-2-like surface reflectance and surface shortwave albedo under different illumination and viewing geometry conditions.

We simulated Sentinel-2-like surface reflectance in several steps. First, we split the complete datasets of 7200 MODIS BRDF data of 16 land cover types into training and validating components, with 400 and 50 samples (Fig. 1) for each land cover type. Second, we divided the illumination and geometry into small angular bins, and simulated MODIS-like surface reflectance across seven spectral bands for each angular bin using the MODIS BRDF data together with the linear RossThick-LiSparseR BRDF model with Eq. (1) as follows (Lucht et al. 2000):

$$\rho\left(\theta_s,\theta_v,\varphi,\lambda\right)=f_{iso}\left(\lambda\right)+f_{geo}\left(\lambda\right)k_{geo}\left(\theta_s,\theta_v,\varphi\right)+f_{vol}\left(\lambda\right)k_{vol}\left(\theta_s,\theta_v,\varphi\right) \quad (1)$$

where $\rho\ (\theta_s, \theta_v, \varphi, \lambda)$ is surface reflectance under the solar zenith angle of θ_s, viewing zenith angle of θ_v, and relative azimuth angle of φ at the wavelength of λ; k_{geo} and k_{vol} are the geometric optical and volumetric

Table 1
Information of flux sites used for validation, including site name, latitude, longitude, elevation, land cover type, tower height, footprint, slope, the mean coefficient of variation (CV) during the leaf on and leaf off seasons, temporal range, and network. Land cover types are derived from the IGBP classification scheme, including barren sparse vegetation (BSV), cropland (CRO), deciduous broadleaf forest (DBF), evergreen broadleaf forest (EBF), evergreen needleleaf forest (ENF), grassland (GRA), mixed forest (MF), open shrubland (OSH), savanna (SAV), snow and ice (SNO), wetland (WET), and woody savanna (WSA).

Site name	Latitude (°)	Longitude (°)	Elevation (m)	Land cover type	Tower height (m)	Foot print (m)	Slope (°)	CV	Temporal range	Network
US-A10	71.32	−156.61	4	BSV	10	126.28	1.53	2 %	2018–2019	AmeriFlux
US-An1	68.99	−150.28	600	OSH	2.5	31.57	2.86	8 %	2018–2019	AmeriFlux
US-An2	68.95	−150.21	600	OSH	2.5	31.57	0.88	10 %	2018–2019	AmeriFlux
US-An3	68.93	−150.27	600	OSH	2.5	31.57	2.26	5 %	2018–2019	AmeriFlux
US-Arm	36.61	−97.49	314	CRO	2	25.26	0.67	9 %	2018–2020	AmeriFlux
US-Bi1	38.1	−121.5	−3	CRO	2.76	34.85	0.04	6 %	2018–2019	AmeriFlux
US-Brg	39.22	−86.54	180	GRA	10	126.28	7.32	10 %	2018–2020	AmeriFlux
US-Dfc	43.34	−89.71	265	CRO	10	126.28	2.07	4 %	2019	AmeriFlux
US-Edn	37.62	−122.11	−2	WET	10	126.28	0.38	8 %	2018–2019	AmeriFlux
US-Hb3	33.35	−79.23	7	ENF	4.34	54.8	0.55	5 %	2019	AmeriFlux
US-Hbk	43.94	−71.72	367	DBF	34	429.34	4.16	7 %	2018–2020	AmeriFlux
US-Hn3	46.69	−119.46	120.9	OSH	10	126.28	17.73	5 %	2018	AmeriFlux
US-Ib2	41.84	−88.24	227	GRA	2.3	29.04	0.49	3 %	2018	AmeriFlux
US-Jo2	32.58	−106.6	1469	OSH	5	63.14	1.67	5 %	2018–2019	AmeriFlux
US-Kon	39.08	−96.56	417	GRA	3	37.88	1.54	6 %	2018	AmeriFlux
US-Ks3	28.71	−80.74	0	WET	10	126.28	0.29	8 %	2018–2019	AmeriFlux
US-Los	46.08	−89.98	480	WET	10.2	128.8	0.40	10 %	2018–2020	AmeriFlux
US-Me2	44.45	−121.56	1253	ENF	33	416.71	5.22	7 %	2018–2020	AmeriFlux
US-Me6	44.32	−121.61	998	ENF	12	151.53	1.09	5 %	2018–2020	AmeriFlux
US-Mpj	34.44	−106.24	2138	OSH	8.8	111.12	3.17	9 %	2018–2019	AmeriFlux
US-Nc2	35.8	−76.67	5	ENF	22.9	289.17	1.00	8 %	2018–2019	AmeriFlux
US-Nc3	35.8	−76.66	5	ENF	24	303.06	1.12	6 %	2018–2019	AmeriFlux
US-Nc4	35.79	−75.9	1	WET	17	214.67	0.36	3 %	2018–2019	AmeriFlux
US-Ngb	71.28	−156.61	5	SNO	10	126.28	0.49	6 %	2018–2019	AmeriFlux
US-Ngc	64.86	−163.7	35	GRA	10	126.28	2.09	1 %	2018–2019	AmeriFlux
US-Nr1	40.03	−105.55	3050	ENF	25.5	322	9.44	9 %	2018–2019	AmeriFlux
US-Pfb	45.97	−90.32	474	ENF	19	239.92	1.20	8 %	2019	AmeriFlux
US-Pfd	45.97	−90.3	473	WET	9	113.65	0.26	10 %	2019	AmeriFlux
US-Pfg	45.97	−90.27	475	ENF	21	265.18	0.99	9 %	2019	AmeriFlux
US-Pfn	45.94	−90.28	478	DBF	19	239.92	2.01	3 %	2019	AmeriFlux
US-Ro4	44.68	−93.07	274	GRA	3.7	46.72	2.02	2 %	2018–2020	AmeriFlux
US-Ro5	44.69	−93.06	283	CRO	3.7	46.72	1.21	2 %	2018–2020	AmeriFlux
US-Ro6	44.69	−93.06	282	CRO	3.7	46.72	1.21	4 %	2018–2020	AmeriFlux
US-Seg	34.36	−106.7	1622	GRA	2.9	36.62	0.00	4 %	2018–2019	AmeriFlux
US-Ses	34.33	−106.74	1593	OSH	3.2	40.41	7.09	3 %	2018–2019	AmeriFlux
US-Snf	38.04	−121.73	−4	GRA	2.75	34.73	1.82	3 %	2018–2020	AmeriFlux
US-Srg	31.79	−110.83	1291	GRA	2.6	32.83	3.29	3 %	2018–2020	AmeriFlux
US-Srm	31.82	−110.87	1120	WSA	7.1	89.66	2.78	5 %	2018–2020	AmeriFlux
US-Srs	31.82	−110.85	1169	WSA	10	126.28	3.11	4 %	2018	AmeriFlux
US-Ton	38.43	−120.97	177	WSA	23.5	296.75	3.51	7 %	2018–2020	AmeriFlux
US-Tw4	38.1	−121.64	−5	WET	4.5	56.82	0.07	9 %	2018–2020	AmeriFlux
US-Tw5	38.11	−121.64	−5	WET	5	63.14	1.47	5 %	2018–2020	AmeriFlux
US-Uaf	64.87	−147.86	155	ENF	6	75.77	1.64	4 %	2018–2019	AmeriFlux
US-Umd	45.56	−84.7	239	DBF	32	404.08	0.39	10 %	2018–2020	AmeriFlux
US-Var	38.41	−120.95	129	GRA	2.5	31.57	6.09	4 %	2018–2020	AmeriFlux
US-Vcp	35.86	−106.6	2500	ENF	24	303.06	2.55	8 %	2018–2019	AmeriFlux
US-Vcs	35.92	−106.61	2752	ENF	13	164.16	22.86	9 %	2018–2019	AmeriFlux
US-Whs	31.74	−110.05	1370	OSH	2.5	31.57	1.54	3 %	2018–2020	AmeriFlux
US-Wjs	34.43	−105.86	1931	SAV	8	101.02	0.23	8 %	2018–2019	AmeriFlux
US-Wkg	31.74	−109.94	1531	GRA	3	37.88	3.02	7 %	2018–2020	AmeriFlux
US-Xab	45.76	−122.33	363	ENF	19	239.92	4.46	5 %	2018–2020	AmeriFlux
US-Xae	35.41	−99.06	516	GRA	8	101.02	1.61	5 %	2018–2020	AmeriFlux
US-Xba	71.28	−156.62	6	WET	9	113.65	0.35	2 %	2018–2020	AmeriFlux
US-Xcl	33.4	−97.57	259	GRA	22	277.81	5.49	9 %	2018–2020	AmeriFlux
US-Xcp	40.82	−104.75	1654	GRA	9	113.65	0.15	3 %	2018–2020	AmeriFlux
US-Xdc	47.16	−99.11	559	GRA	8	101.02	3.02	4 %	2018–2020	AmeriFlux
US-Xdl	32.54	−87.8	22	MF	42	530.36	1.47	8 %	2018–2020	AmeriFlux
US-Xha	42.54	−72.17	351	DBF	39	492.47	3.87	9 %	2018–2020	AmeriFlux
US-Xhe	63.88	−149.21	705	OSH	9	113.65	3.28	9 %	2018–2019	AmeriFlux
US-Xje	31.19	−84.47	44	ENF	42	530.36	5.70	10 %	2018–2020	AmeriFlux
US-Xjr	32.59	−106.84	1329	OSH	8	101.02	1.99	4 %	2018–2020	AmeriFlux
US-Xka	39.11	−96.61	1329	GRA	8	101.02	1.22	10 %	2018–2020	AmeriFlux
US-Xkz	39.1	−96.56	381	GRA	8	101.02	1.26	5 %	2018–2020	AmeriFlux
US-Xmb	38.25	−109.39	1767	OSH	8	101.02	2.89	10 %	2018–2020	AmeriFlux
US-Xml	37.38	−80.52	1126	DBF	29	366.2	3.00	6 %	2018–2020	AmeriFlux
US-Xng	46.77	−100.92	578	GRA	8	101.02	0.89	4 %	2018–2020	AmeriFlux
US-Xnw	40.05	−105.58	3513	ENF	8	101.02	14.37	6 %	2018–2020	AmeriFlux
US-Xsb	29.69	−81.99	45	ENF	35	441.96	0.44	10 %	2018–2020	AmeriFlux
US-Xse	38.89	−76.56	15	DBF	62	782.91	3.47	10 %	2018–2020	AmeriFlux
US-Xsj	37.11	−119.73	368	SAV	39	492.47	8.66	7 %	2018–2020	AmeriFlux

(*continued on next page*)

Table 1 (*continued*)

Site name	Latitude (°)	Longitude (°)	Elevation (m)	Land cover type	Tower height (m)	Foot print (m)	Slope (°)	CV	Temporal range	Network
US-Xsl	40.46	−103.03	1364	CRO	8	101.02	0.63	6 %	2018–2020	AmeriFlux
US-Xsr	31.91	−110.84	983	OSH	8	101.02	1.34	6 %	2018–2020	AmeriFlux
US-Xst	45.51	−89.59	481	DBF	22	277.81	0.89	10 %	2019–2020	AmeriFlux
US-Xta	32.95	−87.39	135	ENF	35	441.96	14.56	9 %	2018–2020	AmeriFlux
US-Xtl	68.66	−149.37	843	WET	9	113.65	1.16	8 %	2018–2020	AmeriFlux
US-Xwd	47.13	−99.24	579	GRA	8	101.02	1.14	4 %	2018–2020	AmeriFlux
BOS	40.13	−105.24	1689	GRA	10	126.28	1.19	10 %	2018–2020	BSRN
BUD	47.43	19.18	139	GRA	10	126.28	1.65	8 %	2019–2020	BSRN
GCR	34.25	−89.87	98	GRA	10	126.28	0.83	2 %	2018–2020	BSRN
NYA	78.93	11.93	11	GRA	10	126.28	3.56	0 %	2018–2020	BSRN
TAT	36.06	140.13	25	GRA	10	126.28	2.18	9 %	2018–2020	BSRN
BE-Bra	51.31	4.52	16	MF	24	303.06	5.49	7 %	2018/2020	EuropeFlux
BE-Dor	50.31	4.97	247	GRA	10	126.28	3.70	4 %	2018/2020	EuropeFlux
BE-Lon	50.55	4.75	167	CRO	10	126.28	0.93	4 %	2018–2020	EuropeFlux
BE-Vie	50.3	6	493	MF	30	378.83	17.58	9 %	2018–2019	EuropeFlux
CH-Cha	47.21	8.41	393	GRA	10	126.28	1.65	9 %	2018–2019	EuropeFlux
CZ-Wet	49.02	14.77	425	WET	10	126.28	4.24	6 %	2018–2019	EuropeFlux
DE-Geb	51.1	10.91	158	CRO	5	63.14	1.48	5 %	2018/2020	EuropeFlux
DE-Hai	51.08	10.45	459	DBF	10.5	132.59	4.86	9 %	2019	EuropeFlux
DE-Rur	50.62	6.3	512	GRA	10	126.28	3.06	7 %	2018–2020	EuropeFlux
DE-Rus	50.87	6.45	102	CRO	10	126.28	2.94	6 %	2018–2020	EuropeFlux
ES-Lm1	39.94	−5.78	265	SAV	7	88.39	2.42	9 %	2018–2019	EuropeFlux
ES-Lm2	39.93	−5.78	272	SAV	6	75.77	5.22	8 %	2018–2019	EuropeFlux
FR-Mej	48.12	−1.8	39	GRA	10	126.28	2.93	2 %	2020	EuropeFlux
IT-Cp2	41.7	12.36	17	EBF	13	164.16	1.55	5 %	2020	EuropeFlux
IT-Lsn	45.74	12.75	1	OSH	10	126.28	1.85	2 %	2018–2020	EuropeFlux
IT-Mtm	46.69	10.58	1480	GRA	10	126.28	26.56	6 %	2018/2020	EuropeFlux
IT-Ren	46.59	11.43	1748	ENF	25	315.69	14.29	7 %	2019	EuropeFlux
IT-Sr2	43.73	10.29	14	ENF	19	239.92	3.95	10 %	2018–2019	EuropeFlux
IT-Tor	45.84	7.58	2162	GRA	3.5	44.2	18.21	10 %	2018–2020	EuropeFlux
CN-Arou	38.05	100.46	2187	GRA	2.5	31.57	2.20	4 %	2019–2020	HiWaterWSN
CN-Dsl	38.84	98.94	1695	BSV	2.5	31.57	3.66	3 %	2019–2020	HiWaterWSN
CN-Jyl	37.84	101.12	2365	GRA	2.5	31.57	11.78	2 %	2019–2020	HiWaterWSN
CN-Yak	38.01	100.24	2154	GRA	2.5	31.57	10.16	6 %	2019–2020	HiWaterWSN
BON	40.05	−88.37	230	CRO	10	126.28	1.53	4 %	2018–2020	SURFRAD
DRA	36.62	−116.02	1007	OSH	10	126.28	3.01	9 %	2018–2020	SURFRAD
FPK	48.31	−105.1	634	GRA	10	126.28	1.39	9 %	2018–2020	SURFRAD
PSU	40.72	−77.93	376	CRO	10	126.28	0.93	4 %	2018–2020	SURFRAD

scattering kernels respectively characterized by the functions of the illumination and viewing geometry; f_{geo} and f_{vol} are the weights of these two kernel functions; and f_{iso} is the isotropic weight.

Finally, we converted the simulated MODIS-like surface reflectance into the Sentinel-2-like surface reflectance with the band conversion coefficients between these two satellites (Eq. (2) and Fig. S1), which were derived from a linear regression approach using the RSR function profiles of Sentinel-2 and MODIS, together with 2394 samples of high-quality spectral data. These spectra include 815 samples from the Ground Object Background Spectral Library for Surveying and Mapping (GOSPEL) (Zhong et al. 2020), 119 samples from the book of quantitative remote sensing for land surfaces (Liang, 2004), 221 samples from the spectral library of typical objects in China (Wang et al. 2009), 47 samples from the snow spectral datasets in Greenland (Qu et al. 2014), and 1192 samples from the USGS Digital Spectral Library (Clark et al. 2007). Because the Sentinel-2 twin satellites have very similar spectral response curves (Fig. 5), we used the same band conversion coefficients for these two sensors with Eq. (2) as follows:

$$\rho_{S2}\left(\lambda_i\right) = a_{i0} + \sum_{j=1}^{7} a_{ij} \times \rho_{MODIS}\left(\lambda_j\right) \tag{2}$$

where ρ_{S2} (λ_i) is the Sentinel-2-like surface reflectance at spectral band λ_i (i = 1, 2, 3, 4); ρ_{MODIS} (λ_j) is the MODIS-like surface reflectance at spectral band λ_j (j = 1, 2, 3, 4, 5, 6, 7); a_{ij} is the band conversion coefficient from MODIS spectral band λ_j to Sentinel-2 spectral band λ_i; and a_{i0} is the constant coefficient at spectral band λ_i (Table 2). The close agreement between the converted Sentinel-2-like reflectance from MODIS-like reflectance and the directly simulated Sentinel-2-like reflectance suggests a high accuracy of the proposed band conversion coefficients (Fig. S1).

We simulated datasets of shortwave albedo from the MODIS BRDF data in two steps: (1) generating the narrowband albedo of seven MODIS spectral bands by integrating the BRDF data over the illumination or viewing geometry (Lucht et al. 2000; Schaaf et al. 2002). Specifically, we integrated MODIS BRDF data over the viewing hemisphere and the illumination and viewing hemispheres to simulate the BSA and WSA datasets; (2) converting the narrowband albedo to shortwave albedo with the regression coefficients as suggested by Liang et al. (2002).

3.1.2. *Building LUTs from the simulated datasets*

With the pairs of the simulated Sentinel-2-like spectral reflectance and the associated shortwave albedo within the same angular bin, we used the linear regression approach to build the LUTs (i.e. reflectance-albedo relationship) that connect shortwave albedo (both BSA and WSA) with spectral reflectance (He et al. 2018; Qu et al. 2014) using following Eq.3:

$$\alpha = C_0\left(\theta_s, \theta_v, \varphi\right) + \sum_{i=1}^{4} C_i\left(\theta_s, \theta_v, \varphi\right) \times \rho_{S2}\left(\lambda_i\right) \tag{3}$$

where α is the surface shortwave albedo; ρ_{S2} (λ_i) is the Sentinel-2-like surface reflectance at spectral band λ_i (i = 1, 2, 3, 4); and C_i (θ_s, θ_v, φ) denotes the regression coefficient at spectral band λ_i.

We built up the LUTs in three steps. First, we fine-tuned the optimal sizes of the BRDF training sample and angular bin on the LUT building with two sensitivity analyses: (1) with the validating component of the MODIS data, we selected different angular bin sizes for algorithm

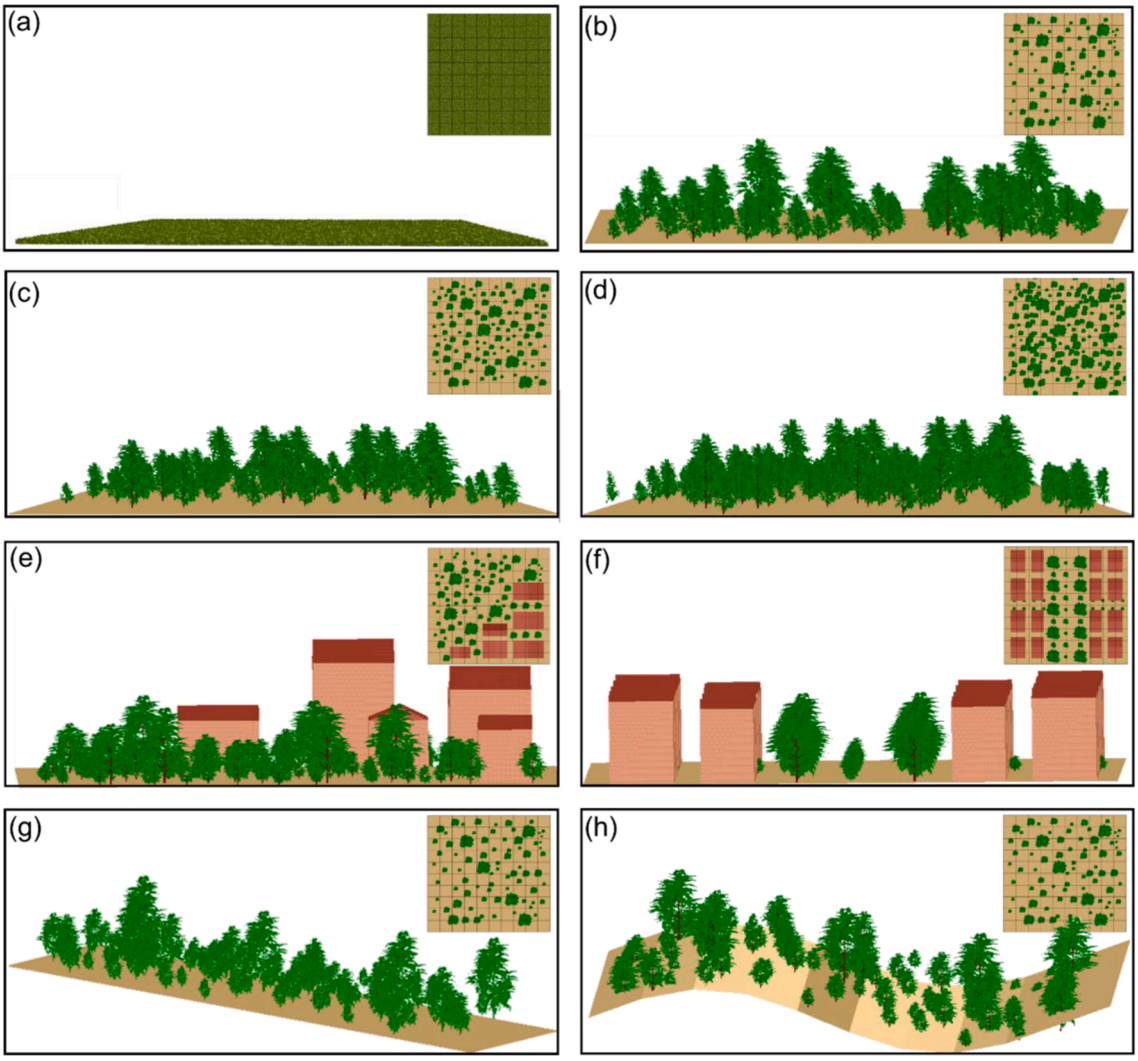

Fig. 3. Lateral views of the Discrete Anisotropic Radiative Transfer (DART)-simulated 100-m × 100-m scenes with a 10-m spatial resolution across different landscape configurations, including **(a)** homogeneous grassland, **(b)** sparse forest, **(c)** medium dense forest, **(d)** dense forest, **(e)** unevenly distributed urban, **(f)** uniformly distributed urban, **(g)** sloping surface, and **(h)** rugged terrain. The aerial views of the DART-simulated scenes are listed as sub-subplots in the top right of each subplot.

training and validation. We found that the angular bin sizes of 2°, 2°, 2°, and 5° for solar zenith angle, viewing zenith angle, solar zenith angle at local solar noon, and relative azimuth angle, respectively, could generate surface albedo with reasonable accuracy (Fig. 6 and Fig. S2), and thus used these optimal angular bin sizes in our algorithm; and (2) with the optimal angular bin size, we selected different BRDF training samples for algorithm training and validation, and found that the total sample size of 6000 could make the proposed algorithm stable with high accuracy (Fig. S3). With the flux measurements as benchmarks, we additionally assessed the effects of training sample representativeness on the final algorithm performance (Fig. S4).

Second, we considered the topographic effects in generating reflectance-albedo LUTs with two assumptions. Firstly, we assumed that the MODIS BRDF parameter product was stable regardless of topography so that it could be used for generating BRDF over slopes. Secondly, we assumed that the topographic effects on 10-m Sentinel-2 surface reflectance were more dominated by the distortions of illumination and viewing geometry than the casting shadows and observation masks and the multiple-scattering among target slope and adjacent slopes (Wen et al. 2018, 2022; Wu et al. 2019). With these two assumptions, we used the local solar-viewing geometry (i.e. relative geometry between slope and solar or viewing sensor) as algorithm inputs to drive the LUTs (Lin et al. 2018, 2021). With the training component of MODIS data, we generated two types of LUTs for the BSA and WSA retrievals.

Finally, we coupled the two LUTs of BSA and WSA with the GEE platform by using the default remap function to search regression coefficients and retrieve surface albedo. It is noteworthy that since regional- and global-scale 10-m digital elevation model (DEM) datasets that spatially match Sentinel-2 resolution are very limited and have not yet been ingested into the GEE platform, we thus set the slope gradients to zero by default in our following regional and global albedo estimation and analysis, but we particularly considered topographic impacts in the accuracy assessment with 3-D model simulations and tower-based flux measurements.

3.2. *Validating the direct estimation algorithm*

The 3-D DART simulations, ground measurements, and MODIS observations were used to evaluate the accuracy of Sentinel-2-derived surface albedo across three spatial levels ranging from the site, regional, to global scale. We first applied the developed algorithm to the DART simulated Sentinel-2-like reflectance to estimate surface albedo and compared the derived albedo with the DART simulated albedo. We then used this algorithm to estimate surface albedo from Sentinel-2

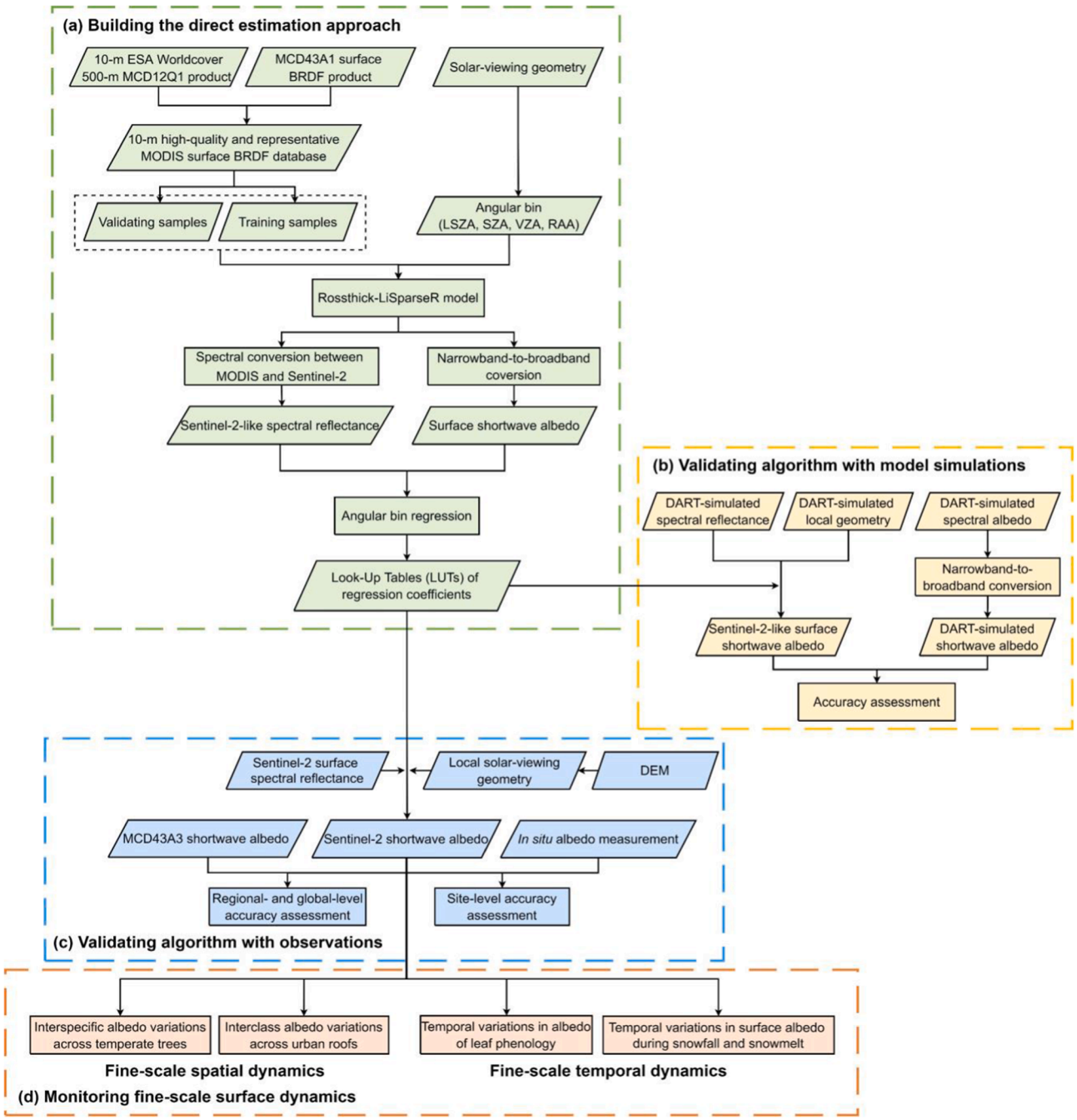

Fig. 4. Flowchart of the algorithm development, evaluation, and application. It includes four major subtasks: **(a)** building the direct estimation approach; **(b)** validating algorithm with model simulations; **(c)** validating algorithm with flux measurements and satellite observations; and **(d)** monitoring fine-scale surface dynamics.

satellite surface reflectance and conducted evaluations with the tower-based flux measurements and MODIS data. Three commonly used metrics were used for accuracy assessments, including the bias, root-mean-square-error (RMSE), and coefficient of determination (R^2).

3.2.1. Estimating surface albedo using the developed LUTs

Pre-built LUTs were used to estimate surface albedo from the DART simulated Sentinel-2-like reflectance data and Sentinel-2 satellite surface reflectance.

(1) **Retrieval of surface albedo from the DART simulated reflectance.** With the DART simulated Sentinel-2-like surface reflectance and solar-viewing geometry, we retrieved surface albedo using the pre-built LUTs in Eq. (3) to estimate both BSA and WSA.

(2) **Retrieval of surface albedo from Sentinel-2 reflectance.** We first used the cloud probability product with the s2cloudless algorithm provided by GEE to remove cloudy and shady Sentinel-2 pixels. With the cloud-free Sentinel-2 reflectance and solar-viewing geometry, we then used them as inputs for the pre-built LUTs in Eq. (3) to estimate both BSA and WSA.

3.2.2. Assessing the proposed algorithm at a 10-m scale

The absolute accuracy and uncertainty of the Sentinel-2-derived albedo were evaluated at a 10-m scale using the DART simulations and flux observations. We first compared the estimated pairs of BSA and WSA using our algorithm with the DART simulation pairs of BSA and WSA (Fig. 7, Figs. S5 and S6). We then compared the blue-sky albedo

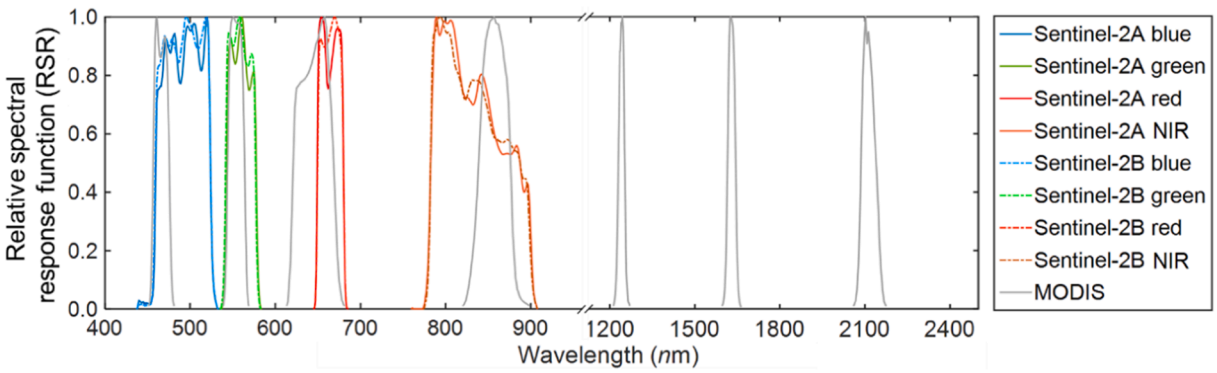

Fig. 5. Relative spectral response (RSR) function profiles of the Sentinel-2 twin (Sentinel-2A and Sentinel-2B) and Moderate-Resolution Imaging Spectroradiometer (MODIS) satellites across different spectral domains, including four narrow spectral bands of blue, green, red, and near-infrared (NIR) for the Sentinel-2 twin satellites and seven narrow spectral bands for the MODIS satellite. The RSR profiles of the MODIS satellite are labeled as gray. The RSR profiles of the Sentinel-2 satellites are displayed as the sky blue, grass green, dark red, and slight yellow for the spectral bands of blue, green, red, and NIR, respectively, including solid lines for Sentinel-2A and dashed lines for Sentinel-2B. (For interpretation of the references to color in this figure legend, the reader is referred to the web version of this article.)

Table 2
Band conversion coefficients a_{ij} between Sentinel-2 and Moderate Resolution Imaging Spectroradiometer (MODIS) satellites, and the associated uncertainties in simulating spectral reflectance.

j / i	0	1	2	3	4	5	6	7	RMSE
1 (Blue)	−0.0004	0.7971	0.1363	0.0722	0.0027	−0.0157	0.0205	−0.0136	0.005
2 (Green)	0.0006	−0.0245	0.9584	0.0711	−0.0062	0.0025	−0.0073	0.0065	0.002
3 (Red)	−0.0013	0.0470	−0.1926	1.1406	0.0054	−0.0015	0.0067	0.0009	0.006
4 (NIR)	−0.0004	−0.0291	0.1795	−0.1307	0.9919	−0.0169	−0.0174	0.0335	0.007

a_{ij} ($i = 1, 2, 3, 4$; $j = 1, 2, 3, 4, 5, 6, 7$) is the conversion coefficient from the jth spectral band of MODIS to ith spectral bands (blue, green, red, and NIR) of Sentinel-2; a_0 is the associated constant coefficient (see Eq. (1)); RMSE refers to root-mean-square-error.

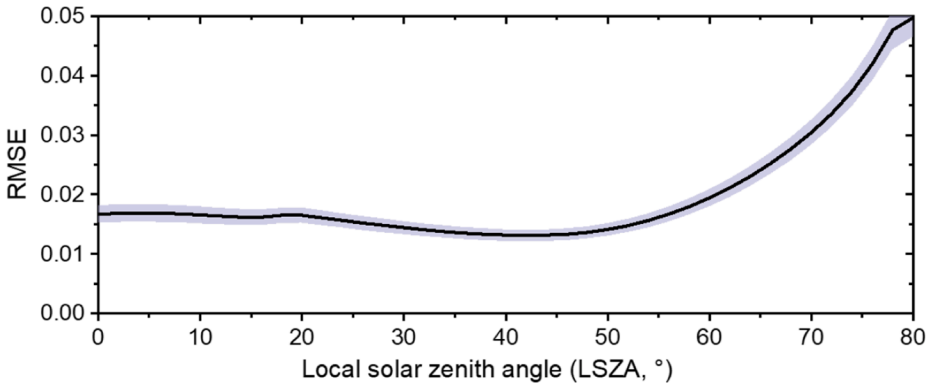

Fig. 6. Sensitivity analysis showing the theoretical accuracies and uncertainties of the proposed direct estimation approach by using the simulated datasets. The root-mean-square-error (RMSE) is derived from the comparison between the LUT-derived albedos and albedo benchmarks of the testing samples. The LUT-derived albedos are estimated from the testing component of reflectance samples together with the proposed LUTs, and the albedo benchmarks are estimated from Moderate-Resolution Imaging Spectroradiometer (MODIS) BRDF data. The solid line and gray buffer refer to the mean and standard deviation of the fitted RMSE, respectively.

derived from the Sentinel-2 observations with the flux measurements, making three considerations: (1) given that flux measurements are a mix of direct and diffuse illumination, we integrated the derived BSA and WSA to calculate blue-sky albedo using the fraction of diffuse skylight in two cases: (i) if the flux site recorded both direct and diffuse fluxes, ground-measured diffuse skylight fraction was used, and (ii) otherwise, a default value of 0.2 was used, according to He et al. (2018); (2) to minimize the potential impacts of unstable illumination on the flux measurements, we selected tower flux measurements between 11:00 a.m. and 1:00 p.m. local time to calculate ground albedo of the local solar noon; and (3) since most tower flux footprints are larger than one Sentinel-2 pixel size, we selected the Sentinel-2 pixels that centered on the tower flux footprint, and conducted the "point-to-pixel" evaluation by comparing ground albedo with the Sentinel-2 centered-pixel albedo (Fig. 8 and Fig. S7), together with a sensitivity analysis to explore the geometric mismatch effects with the 100-time repeated comparisons between ground albedo and the Sentinel-2 pixel observations randomly located within the tower flux footprints (Fig. S8). Third, we assessed the accuracy of the proposed algorithm across different snow cover conditions (Fig. S9), topographic slopes (Fig. S10), flux site networks (Fig. S11), and cross-year variations (Fig. 9, Figs. S12 and S13). We also compared our algorithm with other commonly-used alternatives, including the narrow-to-broadband (NTB) conversion method (Bonafoni and Sekertekin, 2020) and the MODIS-concurrent approach (Li et al. 2018, Fig. S14).

3.2.3. *Assessing the proposed algorithm at a 500-m scale*

Subsequently, we assessed the large-scale mapping capability of the proposed algorithm by comparing the Sentinel-2-derived pairs of BSA and WSA with the MODIS BSA and WSA products at a 500-m scale in two

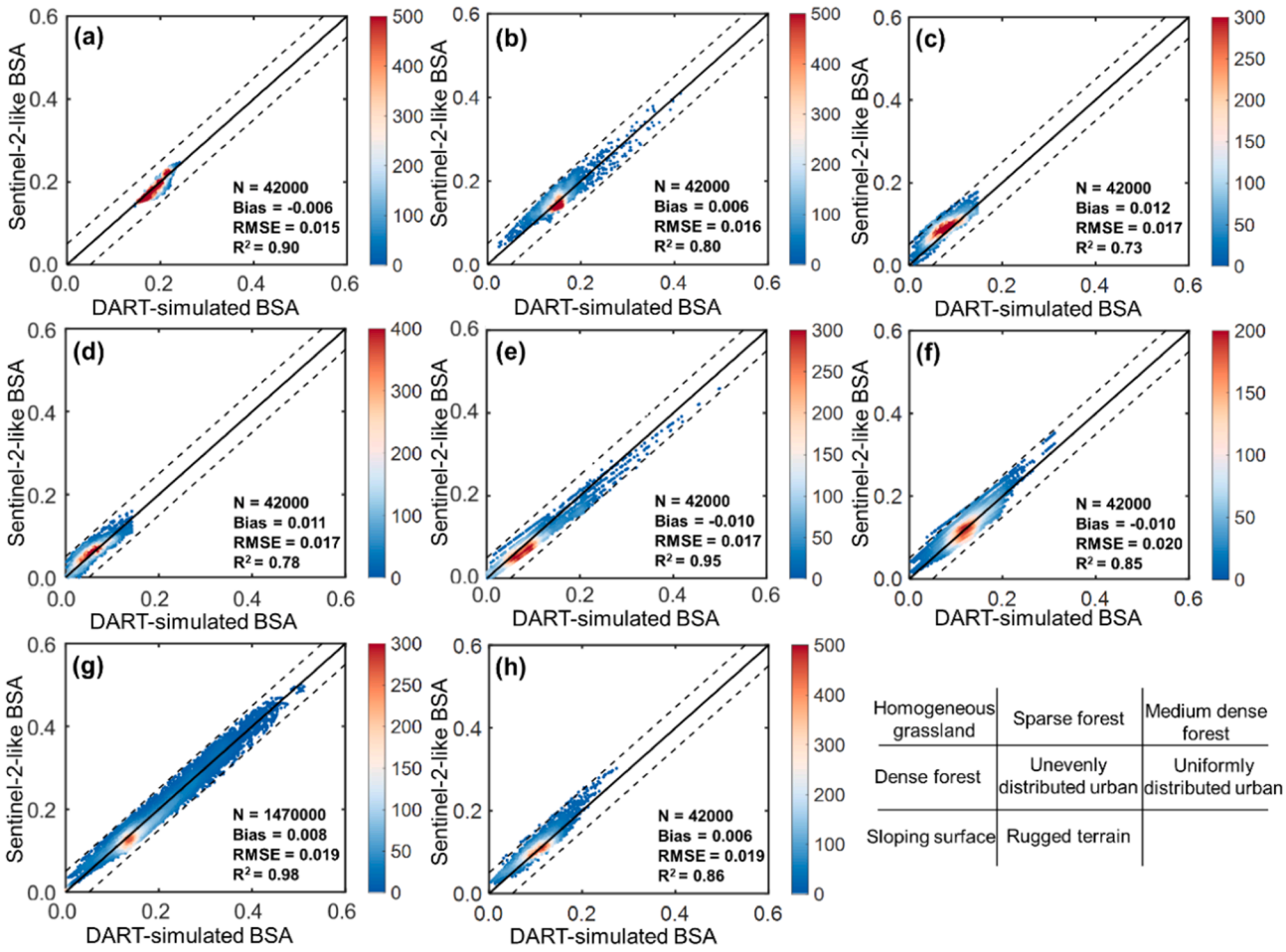

Fig. 7. Accuracy assessments of the proposed algorithm by using the Discrete Anisotropic Radiative Transfer (DART)-simulated black-sky albedo (BSA) across different landscape configurations, including **(a)** homogeneous grassland, **(b)** sparse forest, **(c)** medium dense forest, **(d)** dense forest, **(e)** unevenly distributed urban, **(f)** uniformly distributed urban, **(g)** sloping surface, and **(h)** rugged terrain. N indicates the number of simulated surface albedo used for comparison; Bias is the difference between the pairs of Sentinel-2-like and DART-simulated BSAs; RMSE is the root-mean-square-error; R^2 is the coefficient of correlation. Black solid lines show the 1:1 line. The black dashed lines show the error lines of −0.05 and 0.05 between the Sentinel-2-like BSAs and DART-simulated BSAs.

steps. First, we estimated surface albedos from Sentinel-2 in gridded tiles across 16 land cover types and four seasons (Fig. 2), and compared them with the corresponding MODIS albedo product with strict quality control (quality bit index = 0) for regional-scale assessment (Figs. 10, 11 and Figs. S15-S17). Second, we generated monthly means of global BSA and WSA from Sentinel-2 in June 2019, and compared them with the corresponding monthly means of global MODIS BSA and WSA for global-scale assessment. Specifically, the derived Sentinel-2 albedos were upscaled from their original resolution of 10 m to 500 m to match MODIS data resolution using an area-weighted averaging approach for regional- and global-scale assessments (Figs. 10-12 and Figs. S15-S18).

3.3. Exploring practical applications of Sentinel-2 albedo

We explored the potential of 10-m Sentinel-2 albedo in capturing fine-scale surface dynamics in terms of spatial and temporal characteristics, including two examples of detecting interspecific variations across temperate trees and discriminating interclass differences across urban rooftops, and two examples of monitoring leaf phenology and snow events. Because BSA is very close to WSA, we used the Sentinel-2-derived BSA as examples to demonstrate the practical applications of Sentinel-2 albedo.

3.3.1. Detecting fine-scale spatial dynamics of land surface

(1) **Capturing interspecific variations across temperate trees.** The high resolution of Sentinel-2 improves the capability of mapping tree species and assessing interspecific variations. We used the Sentinel-2-derived albedo to detect interspecific variations of one mixed temperate forest stand in Brandenburg, Germany. This forest stand (53°00′00″—53°00′32″N, 13°46′48″—13°49′19″E, site #q in Fig. 2) spans an area of 3 km × 0.7 km and contains 8 dominant tree species, including *Common red alder, Common sessile oak, Douglas fir, European ash, European beech, European Japanese larch, Norway spruce, and Scots pine* (Fig. 13). More details on the forest compositions of this site can be found in Hemmerling et al. (2021). With the vector maps of dominant tree species from the forest inventory data, we extracted the time series of vegetation albedo across tree species by cropping the estimated Sentinel-2 albedo time series in 2019, and then assessed the interspecific variations (Fig. 13). Using the same approach, we also estimated and presented the results of the 30-m resolution Landsat satellite for comparison.

(2) **Capturing interclass variations across urban roofs.** The ability of high-resolution Sentinel-2 albedo to capture fine-scale characteristics of built-ups was evaluated at one urban site in Beijing, China. This site is located south of Beijing (39°47′35″—39°48′04″N, 116°23′56″—116°24′ 50″E, site #r in Fig. 2) and occupies an approximate 1-km × 1-km area displaying a variety of colored rooftops. With the high-resolution Google Earth imagery, we first visually identified each building roof and manually drew the rooftop map with the region of interest (ROI) of different colors. We then overlapped the manual

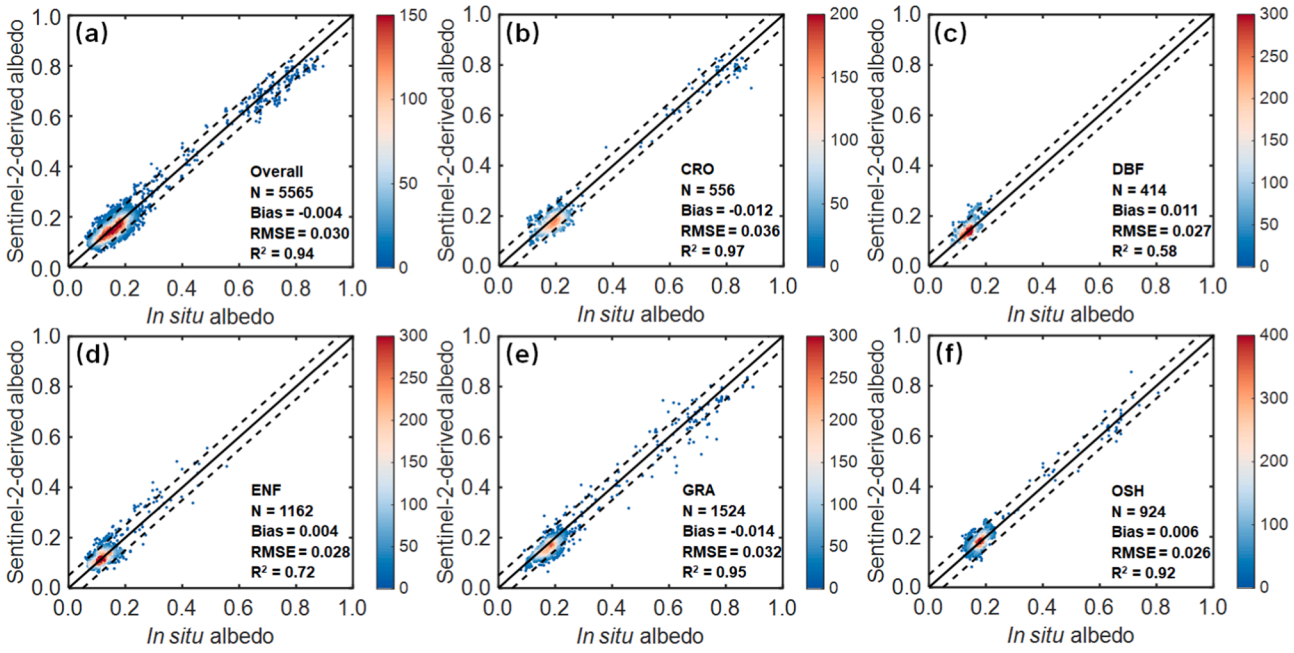

Fig. 8. Site-scale examples showing density scatter plots of the Sentinel-2-derived surface albedo and *in situ* albedo at local flux sites across five land cover types, including **(a)** overall, **(b)** cropland (CRO), **(c)** deciduous broadleaf forest (DBF), **(d)** evergreen needleleaf forest (ENF), **(e)** grassland (GRA), and **(f)** open shrubland (OSH); N indicates the number of Sentinel-2 observations used for comparison; Bias is the difference between the observational pairs of the Sentinel-2-derived and *in situ* albedos; RMSE is the root-mean-square-error; R^2 is the coefficient of correlation. Black solid lines show the 1:1 line. The black dashed lines show the error lines of −0.05 and 0.05 between the satellite data and ground measurements.

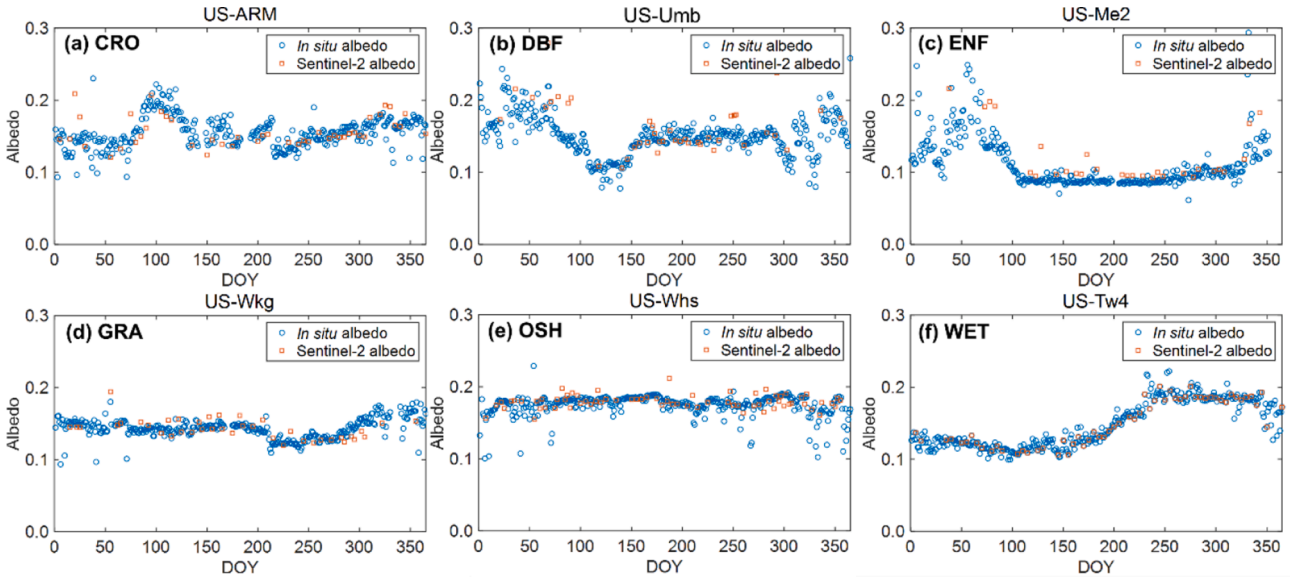

Fig. 9. Site-scale examples showing seasonality comparisons between the Sentinel-2 estimations and *in situ* observations of surface albedo across six land cover types, including **(a)** cropland (CRO), **(b)** deciduous broadleaf forest (DBF), **(c)** evergreen needleleaf forest (ENF), **(d)** grassland (GRA), **(e)** open shrubland (OSH), and **(f)** wetland (WET). The paired data of Sentinel-2 observations that centered on the flux site footprints and ground measurements in 2019 are used here for demonstration.

ROIs with the Sentinel-2 albedo time series in 2019 and extracted the time series of rooftop albedos. We lastly compared the extracted albedos across different urban rooftops (Fig. 14). With the same approach, we also estimated and extracted the Landsat satellite results of rooftop albedos for comparison (Fig. S19).

3.3.2. *Monitoring fine-scale temporal dynamics of land surface*

Two phenocam sites of the National Ecological Observatory Network (NEON) were selected to demonstrate the advantage of Sentinel-2 albedo in monitoring fine-scale temporal trajectory of land surface, including the leaf phenology of one forest site and the snow events of one agricultural site.

(1) Capturing leaf phenology of temperate trees. We evaluated the capability of Sentinel-2 albedo in capturing leaf phenology using the phenocam observations of the Casey Tree Farm in the Blandy Experimental Farm (BLAN) site in Virginia, USA. This forest site (39°02′01″N, 78°02′30″W, site #s in Fig. 2) includes a mix of land-use types, including woodland, tree nurseries, and hay fields. The tower-top RGB (i.e. red,

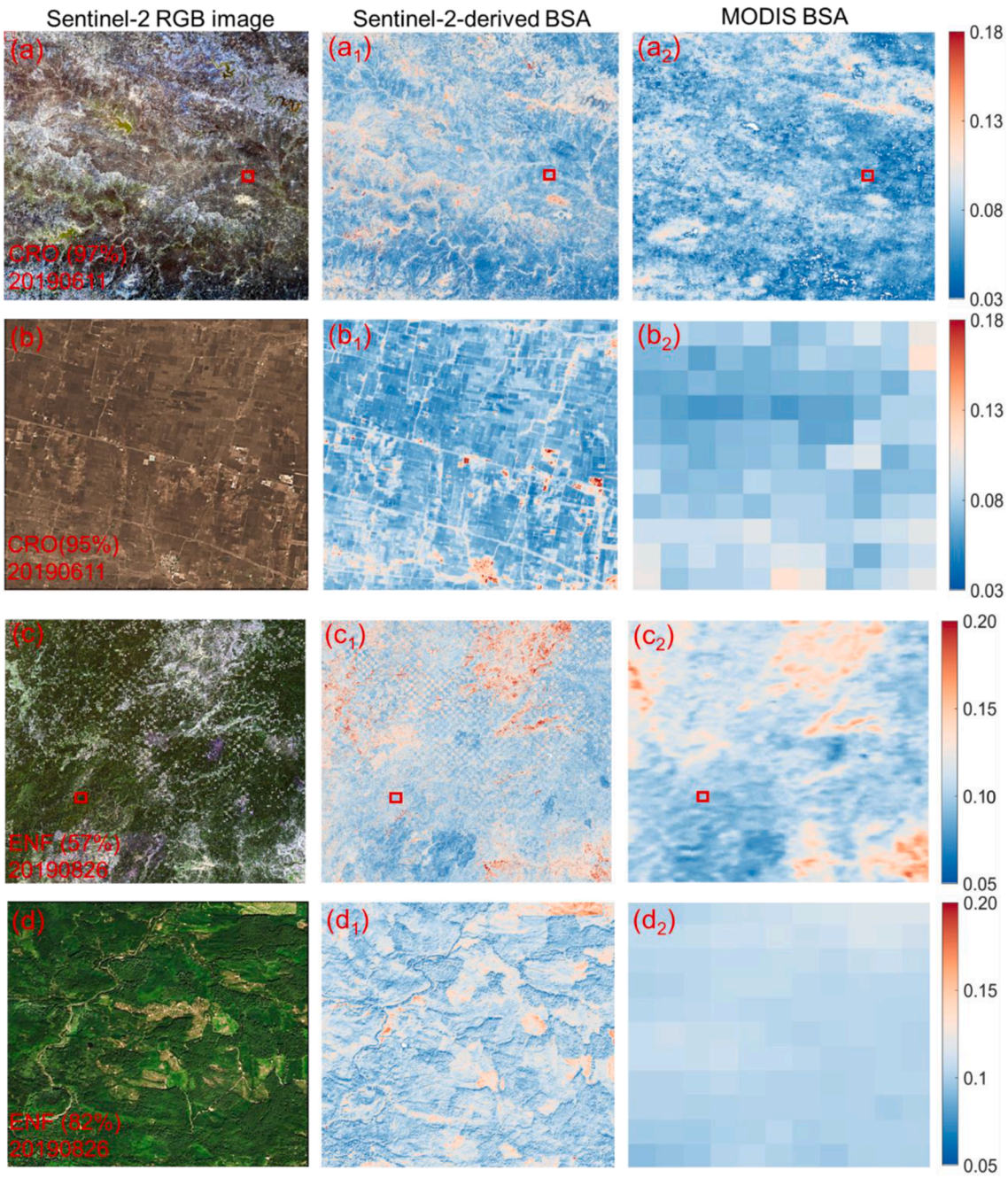

Fig. 10. Regional-scale examples showing the spatial comparisons of surface black-sky albedo (BSA) between Sentinel-2 and Moderate-Resolution Imaging Spectroradiometer (MODIS) satellites across two land cover types, including **(a, b, c, d)** true-color (RGB = red–green-blue) composited Sentinel-2 image, **(a_1, b_1, c_1, d_1)** Sentinel-2-derived BSA, and **(a_2, b_2, c_2, d_2)** MODIS-derived BSA. Panels **(a-a_2)** show the results for cropland (CRO); panels **(b-b_2)** show the results for the subset of the panels **(a-a_2)** that indicated by the red rectangles; panels **(c-c_2)** show the results for evergreen needleleaf forest (ENF); and panels **(d-d_2)** show the results for the subset of the panels **(c-c_2)** that indicated by the red rectangles. The dominant land cover type with the corresponding fractions (in parentheses) were extracted from MCD12Q1, and the observation dates are listed at the bottom left of each Sentinel-2 RGB image. The clear-sky satellite images in summer in 2019 are used here for demonstration. (For interpretation of the references to color in this figure legend, the reader is referred to the web version of this article.)

green, and blue) camera observations of an 8-m flux tower were used to measure leaf phenology dynamics. Using the Sentinel-2 imagery collection in 2019, we first extracted and analyzed the albedo and enhanced vegetation index (EVI) time series of the Sentinel-2 pixel centered on the flux footprint, then compared them with the RGB camera observations (Fig. 15a). We also compared our results with the albedo time series of the Landsat pixel located at the same site.

(2) **Capturing snowfall and snowmelt events.** We assessed the ability of Sentinel-2 albedo in monitoring rapid snowfall and snowmelt events using the phenocam observations of the North Sterling (STER) site in Colorado, USA. This agricultural site (40°27′43″N, 103°01′45″W, site #t in Fig. 2) cultivates a variety of crops, including winter wheat, millet, and maize. We used the tower-top RGB camera observations of an 8-m flux tower to measure cropland dynamics and compared them with the albedo and EVI time series of the central Sentinel-2 pixel within the flux footprint (Fig. 15b). We also compared our results with the albedo time series of the Landsat satellite.

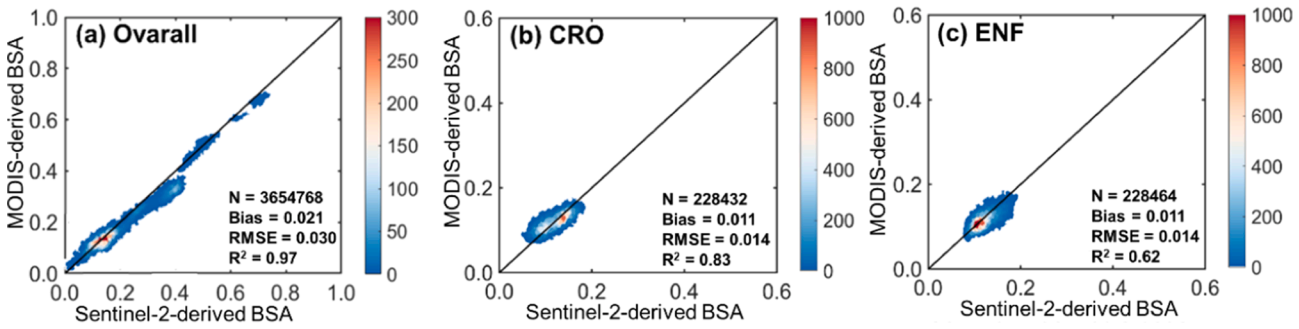

Fig. 11. Regional-scale examples showing the density scatter plots of the Sentinel-2 and Moderate-Resolution Imaging Spectroradiometer (MODIS) black-sky albedo (BSA) across different gridded tiles with two distinct dominant land cover types in 2019, including **(a)** overall, **(b)** cropland (CRO), and **(c)** evergreen needleleaf forest (ENF). The Sentinel-2 and MODIS data across four seasons of spring, summer, fall, and winter in 2019 (one image per season) are used to calculate the averaged surface albedo. The Sentinel-2-derived BSA is resampled from the original resolution of 10 m to the 500-m spatial resolution of MODIS for cross-comparison. N indicates the number of Sentinel-2 observations used for comparison; Bias is the difference between the observational pairs of Sentinel-2-derived and MODIS BSAs; RMSE is the root-mean-square-error; R^2 is the coefficient of correlation.

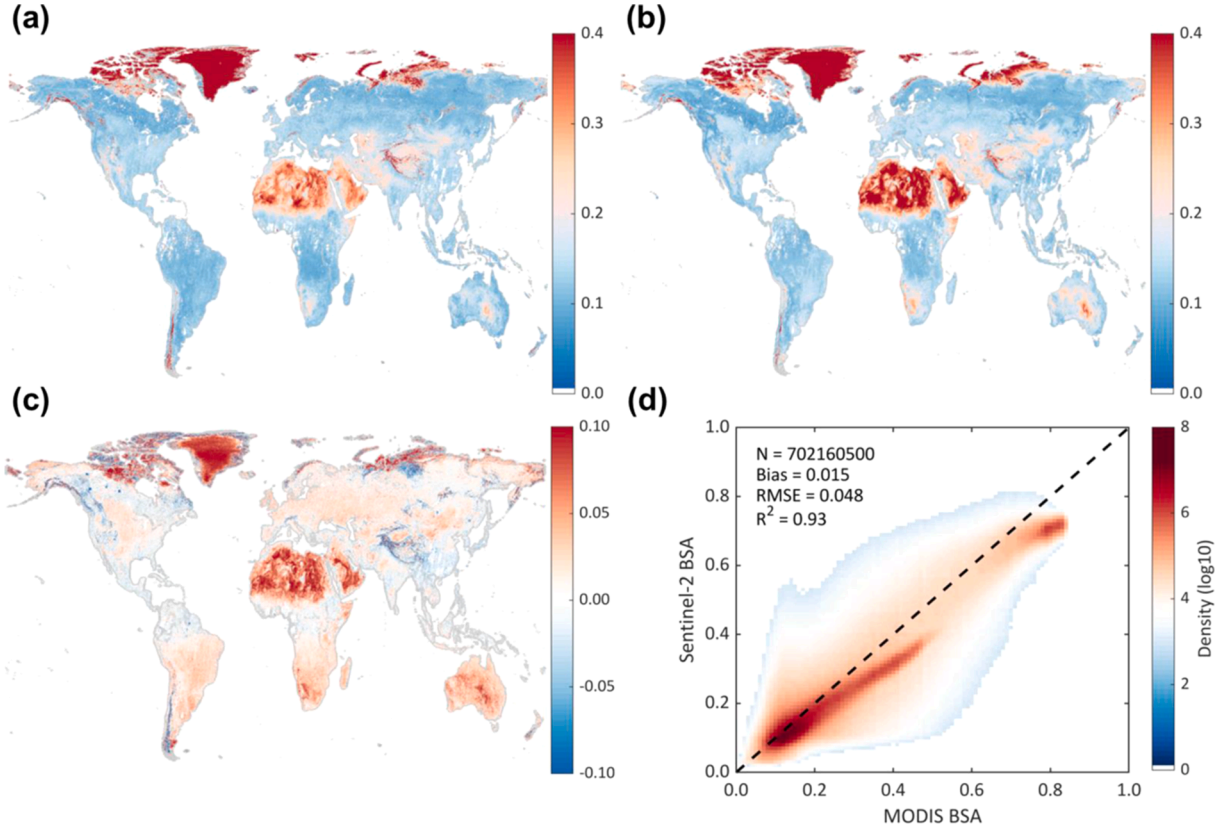

Fig. 12. Global-scale maps of spatial variation in monthly mean of black-sky albedo (BSA) in June 2019, including **(a)** 500-m aggregated Sentinel-2-derived BSA, and **(b)** 500-m Moderate-Resolution Imaging Spectroradiometer (MODIS)-derived BSA. **(c)** the difference between the MODIS-derived BSA and aggregated Sentinel-2-derived BSA; and **(d)** density scatter plot of MODIS-derived BSA and aggregated Sentinel-2-derived BSA. The result of Antarctica is not shown here as there were not available Sentinel-2 observations in June 2019.

4. Results

4.1. Uncertainty of the direct estimation approach

We assessed the theoretical accuracy and uncertainty of the proposed direct estimation approach using the validating component of the MODIS sampling data. As shown in Fig. 6, the mean of the fitted RMSE in simulating shortwave albedo increased from 0.017 to 0.050 when the local solar zenith angle increased from 0° to 80°. Specifically, the mean RMSE was less than 0.020 when the local solar zenith angle was lower than 60°, which suggests the high accuracy of the proposed approach for estimating surface albedo from Sentinel-2 satellites. Our results showed that the direct estimation approach is relatively insensitive to the changes in angular bin size of illumination and viewing geometry (Fig. S2), with slight increases in the maximum RMSEs of 0.035, 0.025, and 0.019 for an increasing bin size from 0° to 40° for the local solar zenith angle, solar zenith angle, and relative azimuth angle, respectively. Our results also showed that algorithm accuracy increased with the size of the BRDF training samples (Fig. S3), with the mean RMSE ranging from 0.056 to 0.017 for an increasing sample size from 500 to 6000 and remaining stable when the sample size was larger than 6000. With flux measurements as benchmarks, our results further revealed

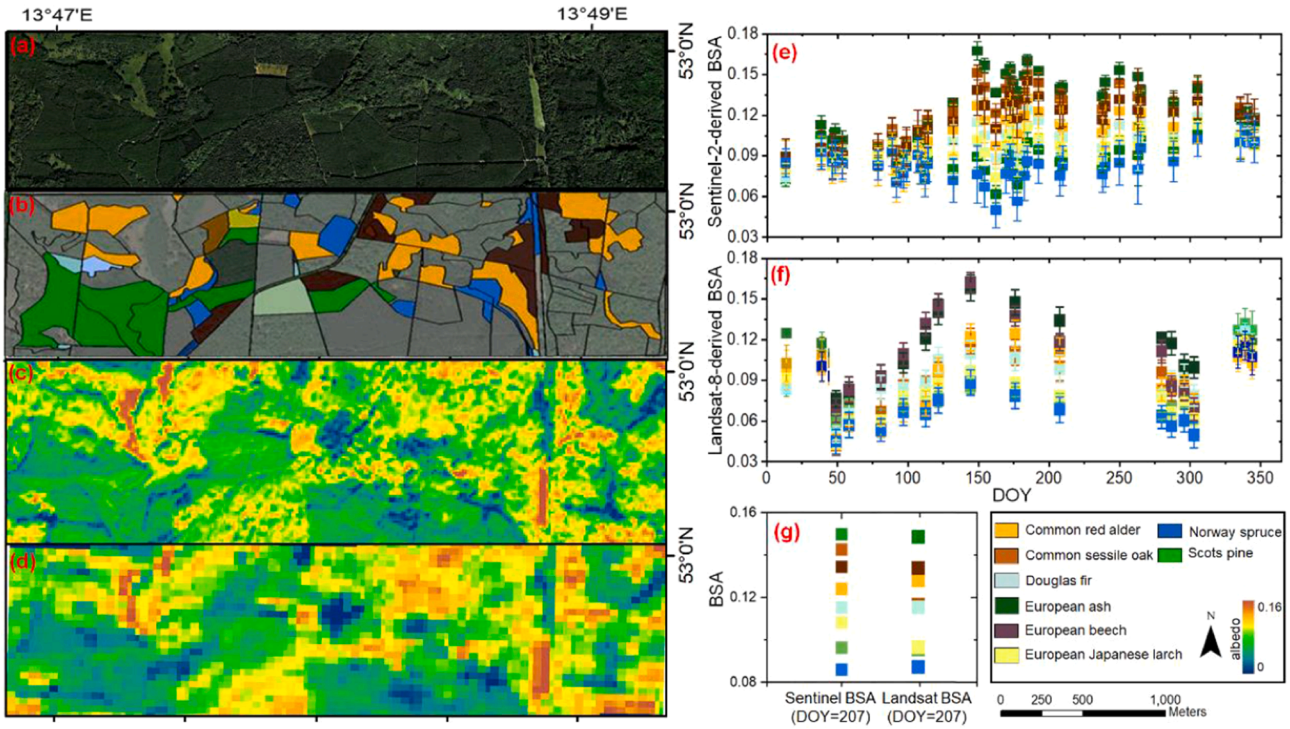

Fig. 13. Examples showing the capability of the Sentinel-2 albedo in capturing interspecific variations, including **(a)** high-resolution true-color (RGB = red–green-blue) composited imagery from Google Earth in 2019, **(b)** dominant tree species based on forest inventory data, **(c)** Sentinel-2-derived albedo, **(d)** Landsat-8-derived albedo, **(e)** time series of Sentinel-2-derived albedo across tree species, **(f)** time series of Landsat-8-dereived albedo across tree species, and **(g)** comparisons between Sentinel-2- and Landsat-8-derived albedo on the same day. Panels **(a)** and **(b)** are adapted from Hemmerling et al. 2021. BSA refers to black-sky albedo. (For interpretation of the references to color in this figure legend, the reader is referred to the web version of this article.)

that increasing the representativeness of BRDF training samples can significantly improve algorithm performance (Fig. S4).

4.2. 10-m scale accuracy assessment of the direct estimation approach

The absolute accuracy of the proposed direct estimation approach in estimating surface albedo from Sentinel-2 was evaluated against the 3-D DART simulations and ground measurements from local flux sites. When compared with the DART simulations, the direct estimation approach presented high accuracy across different landscape configurations (bias = -0.010–0.012, RMSE = 0.015–0.020, R^2 = 0.73–0.98 for BSA; bias = -0.010–0.010, RMSE = 0.014–0.022, R^2 = 0.70–0.97 for WSA; overall RMSE = 0.018, overall bias = 0.005, overall R^2 = 0.88; Fig. 7 and Fig. S5). The low pixel-scale RMSE map also suggests the high accuracy of the direct estimation approach (Fig. S6). When compared with ground measurements, as shown in Fig. 8, the ground flux towers detected significant variations in surface albedo with ranges from 0.065 to 0.907 across different land cover types. Our results demonstrated that the Sentinel-2 satellite accurately captures variations in surface albedo, showing an overall high agreement with ground measurements across all flux sites (bias = -0.004, RMSE = 0.030, R^2 = 0.94) and different land cover types (bias = -0.023–0.011, RMSE = 0.015–0.042, R^2 = 0.40–0.99; Fig. 8, Figs. S7 and S8). Our results also showed that the Sentinel-2 satellite closely tracked albedo variations over snow-free and snow-covered surfaces (bias = -0.003, RMSE = 0.027, and R^2 = 0.62 for snow-free surface; bias = -0.009, RMSE = 0.060, R^2 = 0.84 for snow-covered surface; Fig. S9), flat and rugged slopes (bias = -0.004, RMSE = 0.029, R^2 = 0.94 for slope less than 5°; bias = -0.006, RMSE = 0.031, R^2 = 0.96 for 5°< slope less than 10°; and bias = 0.003, RMSE = 0.040, R^2 = 0.97 for slope greater than 10°; Fig. S10), flux networks (Fig. S11), and cross-year dynamics (Figs. S12 and S13). Our sensitivity analysis results regarding the geometric match effects between flux footprint and Sentinel-2 pixel show the feasibility of the proposed evaluation strategy for selecting representative flux sites and conducting direct comparisons (bias = -0.005–0.006, RMSE = 0.028–0.035, R^2 = 0.82–0.98; Fig. S8). The sensitivity analysis of model comparisons showed a better performance of the proposed direct estimation approach compared with similar alternatives (i.e. the NTB conversion method and MODIS-concurrent approach; Fig. S14).

Our evaluations show that Sentinel-2 and flux tower observations detected significant seasonality in surface albedo caused by leaf phenology or surface changes across different land cover types (Fig. 9). Deciduous broadleaf forest (DBF) exhibited a leaf phenology-driven seasonality with increasing albedo for the green-up stage and decreasing albedo for the leaf senescence stage (Fig. 9b). Evergreen forest (ENF) showed a relatively stable albedo pattern across seasons except for the increasing pattern in spring and winter due to snowfall events (Fig. 9c). In contrast, cropland (CRO) displayed a human-driven seasonality with many variabilities in albedo that might have been disturbed by management activities (e.g. increasing albedo patterns in the growing phase augmented by decreasing soil moisture and abrupt drops in albedo magnitude caused by irrigation practices; Fig. 9a). Wetland presented an increasing albedo seasonality likely due to decreasing seasonal soil moisture (Fig. 9f). Compared with the other land cover types, grassland (GRA) and open shrubland (OSH) showed far fewer albedo variations across seasons (Fig. 9d-e). Our results also showed that the surface albedos derived from Sentinel-2 have similar seasonality patterns with the ground measurements across different land cover types (Fig. 9) and inter-annual cycles (Fig. S13).

4.3. 500-m scale accuracy assessment of the direct estimation approach

We evaluated the capability of the proposed direct estimation approach in large-scale albedo mapping by comparing the Sentinel-2-derived surface albedo with MODIS albedo product across both individual gridded tile and global coverage. As shown in Fig. 10a-a2, 10c-c2,

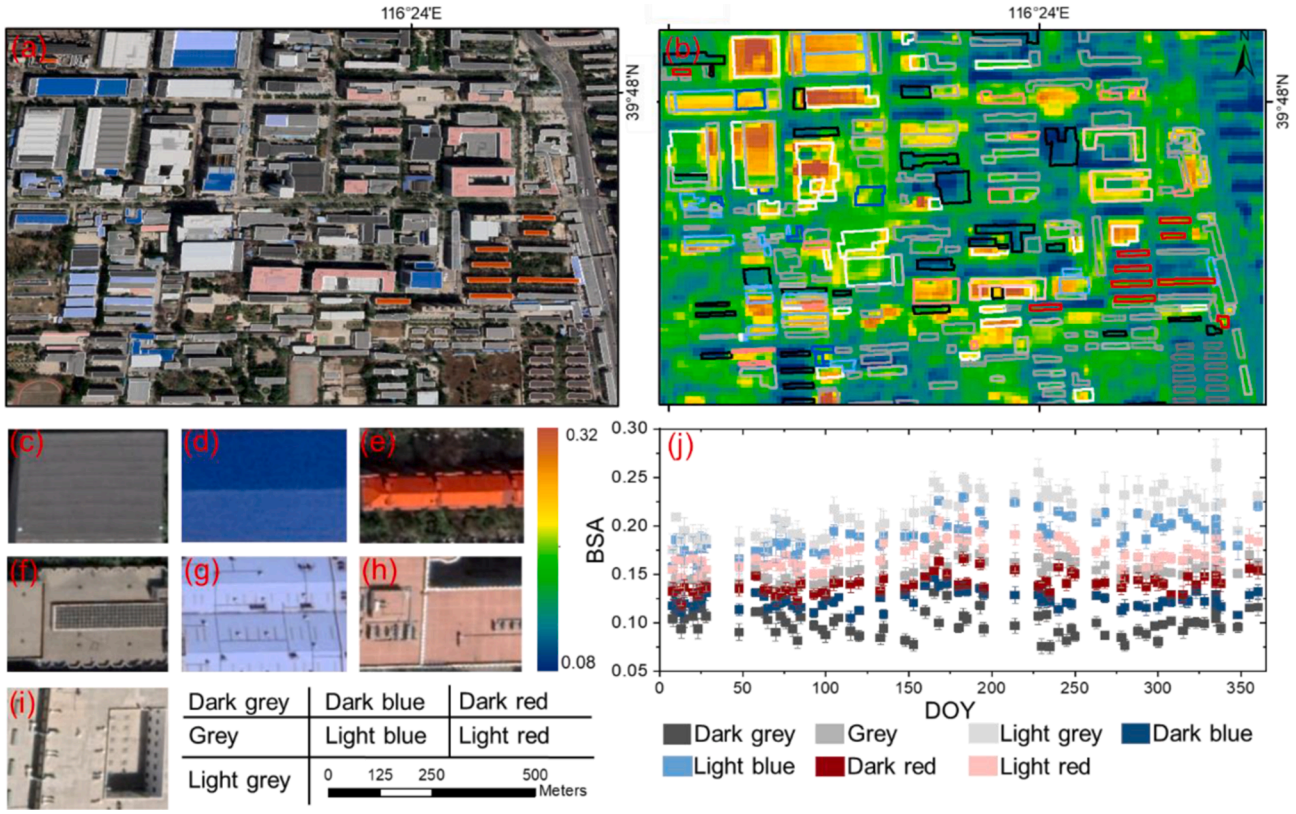

Fig. 14. Examples showing the capability of the Sentinel-2 black-sky albedo (BSA) in detecting urban rooftops, including **(a)** high-resolution true-color (RGB = red–green-blue) composited imagery from Google Earth in 2019; **(b)** Sentinel-2-derived BSA, **(c-i)** examples of the building rooftops with different colors, **(j)** time series of Sentinel-2 BSA across building roofs. The rooftop boundaries in panels **(a)** and **(b)** are visually identified from high-resolution Google Earth imagery. (For interpretation of the references to color in this figure legend, the reader is referred to the web version of this article.)

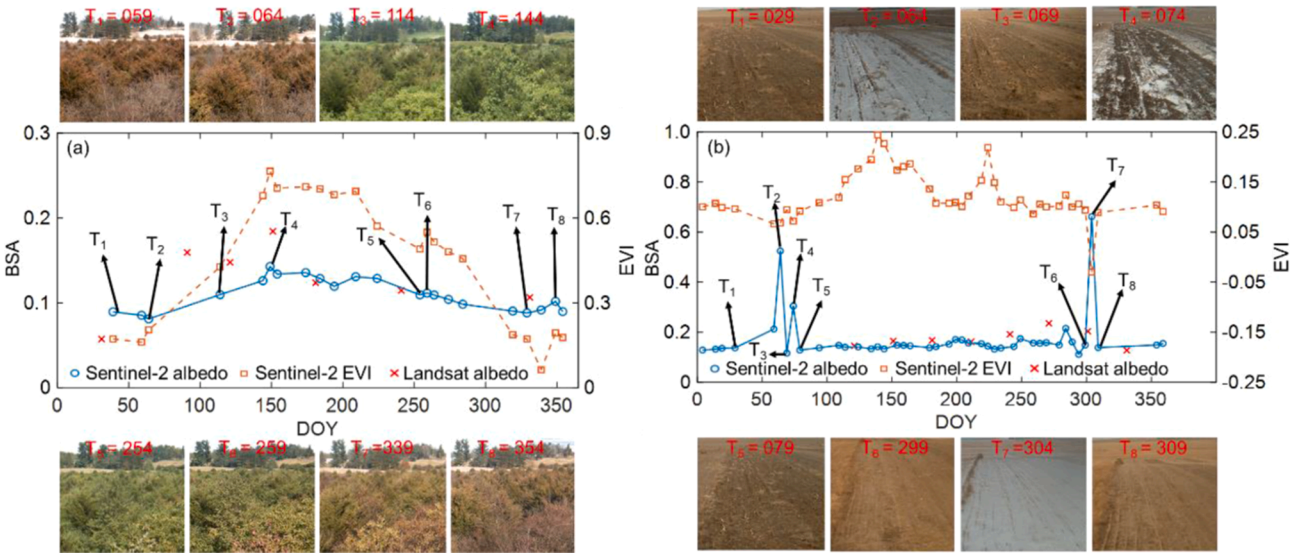

Fig. 15. Examples showing the capability of the Sentinel-2 black-sky albedo (BSA) in monitoring surface temporal dynamics, including **(a)** leaf phenology; and **(b)** snowfall and snowmelt events. The Landsat albedo and Sentinel-2 enhanced vegetation index (EVI) are shown for comparison. T_i (i = 1, 2, 3, 4, 5, 6, 7, and 8) is observation date.

and Fig. S15, both the Sentinel-2 and MODIS gridded tiles showed large variations in the extracted surface albedo across spatial regions and different land cover types. Compared with the MODIS albedo with a relatively coarse resolution of 500 m, our local zoom-in results show that Sentinel-2 detected much more detail on the spatial characteristics of surface albedo in specific regions, such as the heterogeneous agricultural mosaics of cropland (Fig. 10b-b2) and disturbance patches of evergreen forest (Fig. 10d-d2). The 500-m scale assessment results show that the surface albedos derived from Sentinel-2 were overall comparable with the albedos derived from MODIS across gridded tiles (bias = 0.021, RMSE = 0.030, R^2 = 0.97; Fig. 11a) and different land cover types (bias = 0.008–0.048, RMSE = 0.011–0.060, R^2 = 0.47–0.98; Fig. 11b-c and

Fig. S16). Our results also showed the high consistency between Sentinel-2- and MODIS-derived BSA and WSA (bias = 0.008, RMSE = 0.013, R^2 = 0. 81 for BSA; bias = 0.010, RMSE = 0.16, R^2 = 0.77 for WSA; Fig. S17).

Our global-scale comparison maps of two satellites presented similar spatial patterns in surface albedo, with large albedos at the North Pole covered by permanent snow (e.g. Greenland), African regions and Australia characterized by desert or dryland, and mountainous areas of the North American Cordillera, Andes, Appalachians, Alps, and Himalayas (Fig. 12a-b and Fig. S18a-b). Our results also showed close spatial consistency between pixel-level Sentinel-2 and MODIS albedos, with a maximum bias of less than 0.02 across 45.9 % of the global areas (Fig. 12c and Fig. S18c). Overall, the Sentinel-2-derived surface albedos were highly comparable with those from MODIS at the global scale (bias = 0.015, RMSE = 0.048, R^2 = 0.93 for both BSA and WSA; Fig. 12 and Fig. S18).

4.4. Fine-scale surface dynamics from Sentinel-2-derived albedo

We assessed the potential of the Sentinel-2 albedo for monitoring tree albedo variations, discriminating built-ups, and capturing leaf phenology and snow events. We first mapped the pixel-scale albedos of Sentinel-2 and Landsat over the forest stand (Fig. 13). These maps showed that there were large spatial variations in the estimated albedo across the entire landscape, with higher values in the northern and eastern regions and lower values in the southern and western regions (Fig. 13c-d). Due to the higher spatial resolution, Sentinel-2 albedo exhibited many more spatially heterogenous characteristics than Landsat albedo (Fig. 13c vs Fig. 13d). When overlapping these albedo maps with the dominant tree species map (Fig. 13b), we quantified the albedo variations at the interspecific and intraspecific levels and found large seasonal variations within and across tree species (Fig. 13e-g). At the interspecific level, our results showed that *European ash* has the largest species-level mean albedo, followed by *Common sessile oak, European beech, Common red alder, Douglas fir, European Japanese larch, Scots pine, and Norway spruce*. At the intraspecific level, our results showed that *European beech* has the largest variability (indicated by the standard deviation of albedo within the same species), followed by *Norway spruce*, *Common red alder*, *Common sessile oak, Douglas fir, European Japanese larch, Scots pine, and European ash.* Our comparative results between these two satellites demonstrated that Sentinel-2 has many more frequent observations than Landsat (observation number of 43 vs 13 within a one-year cycle) and can detect both interspecific and intraspecific albedo variations, while Landsat shows less capability in detecting intraspecific albedo variations (Fig. 13e vs Fig. 13f).

We then mapped the pixel-scale albedos of Sentinel-2 over the built-up area (Fig. 14). The resulting map showed large spatial variations of the estimated albedo across the entire urban area, with observed higher values over the light-colored rooftops and lower values over the dark-colored rooftops. By overlapping the albedo results with the manual rooftop map, we quantified the albedo variations within and across colors, and found that the light-colored rooftops showed larger class-level mean albedo and within-class albedo variations (indicated by the standard deviation of albedo within the same color) than the dark-colored rooftops (Fig. 14b vs Fig. 14j). Our results also showed a greater potential of Sentinel-2 relative to Landsat in discriminating different colored urban roofs due to the larger interclass Sentinel-2-derived albedo variability (Fig. 14 vs Fig. S19).

Lastly, we extracted and analyzed the albedo and EVI time series over the forest and agricultural sites. As shown in Fig. 15, phenocam RGB images clearly illustrated the key stages of leaf phenology and snowfall and snowmelt events. The extracted Sentinel-2 EVI showed two different seasonality patterns between forest and cropland. The value of forest EVI remained low during the dormant period (i.e. timing T_1 to T_2), increased in the leaf green-up phase (i.e. timing T_2 to T_4) previous to the stable leaf peak stage (i.e. timing T_4 to T_5), decreased in the leaf senescence phase (i.e. timing T_5 to T_7), and reverted back to the dormant stage (i.e. timing T_7 to T_8, Fig. 15a). By contrast, cropland EVI presented more rapid leaf green-up and senescence stages with a double-cropping cycle within one year (Fig. 15b). When comparing the temporal dynamics between EVI and albedo, as shown in Fig. 15a, Sentinel-2 albedo closely tracked EVI seasonality with an increasing pattern during the leaf green-up stage and a decreasing pattern during the leaf senescence stage, suggesting the potential of using Sentinel-2 in monitoring phenology-related biophysical processes. Additionally, Sentinel-2 albedo demonstrated its capability of capturing the rapid temporal trajectory of snow events with different snowfall magnitudes. For example, as shown in Fig. 15b, Sentinel-2 albedo detected a total of three snowfall and snowmelt events (i.e. timing T_1-T_3, T_3-T_5, and T_6-T_8). Due to the relatively lower temporal resolutions, Landsat albedo presented fewer informative observations on leaf phenology and snow events.

5. Discussion

The accurate monitoring of fine-scale surface albedo over large spatial coverages has fostered increasing research interests. However, large uncertainties remain in estimating the fine-scale surface albedo from current satellites due to their coarse spatial and temporal resolutions (Li et al. 2018; Qu et al. 2014; Shuai et al. 2014; Wang et al. 2018). We addressed this challenge by integrating the high-resolution Sentinel-2 images with an improved direct estimation approach. Our approach allows for direct albedo estimation from Sentinel-2 reflectance without the comprehensive retrieval of physical BRDF models requiring multi-angular observations within a short time. Using this approach, we found that Sentinel-2 albedo agreed well with the DART simulations, ground measurements, and MODIS satellite product, and accurately detected the spatial–temporal trajectory of land surface at a 10-m scale. These multi-faceted evaluations demonstrate the great feasibility of using Sentinel-2 data for mapping fine-scale surface albedo to advance our understanding of multiple biophysical and biogeochemical processes.

Our proposed approach is similar to the previous direct estimation model framework, but introduces further advances. As similarly done in previous studies (He et al. 2018; Liang et al. 1999; Qu et al. 2014; Zhang et al. 2020b), we used the BRDF/albedo data of a coarse-resolution satellite to pre-train the reflectance-albedo relationship. Differently, we included additional information on high-resolution land cover to ensure sample representativeness and considered topographic impacts to improve the model's applicability over rugged areas. Moreover, our study presents three additional advancements. First, it is one of the few studies that estimate surface albedo from optical satellites at such a high spatial resolution. Previous studies have primarily focused on satellites with coarse spatial resolution ranging from several hundred meters (e.g. MODIS and VIIRS; Liu et al. 2017; Wang et al. 2018; Wu et al. 2017; Zhou et al. 2016) to tens of meters (e.g. Landsat; Baldinelli et al. 2017; Franch et al. 2014; He et al. 2018; Shuai et al. 2011). Although Sentinel-2 alone, or together with Landsat, has been previously used for estimating surface albedo in agricultural and grassland ecosystems (Li et al. 2018), urban environments (Baldinelli et al. 2017; Guo et al. 2022), and tropical forests (Franch et al. 2018), the generalizable albedo estimation approach over random land covers for Sentinel-2-similar satellites with few angular observations and spectral band configurations has rarely been explored. Second, topography significantly impacts surface albedo (Hao et al. 2018; Ma et al. 2022; Wu et al. 2018), but has rarely been integrated in the albedo retrieval algorithm. In our approach, we accounted for the topographic effects and assessed these effects using both DART simulations and ground measurements. Third, to the best of our knowledge, this study is the first attempt to integrate the direct estimation approach with GEE cloud-computing to enable large-scale computation capability. Our experiments show that estimating surface albedo of one Sentinel-2 gridded tile (*c.* 110 km × 110 km) with the GEE service requires only a few minutes (i.e. 3–10 min), which suggests the

promising possibility of generating a global, 10-m surface albedo product.

Our examples of Sentinel-2 albedo applications demonstrate the great potential of using the proposed approach or data to advance albedo-related fields. Firstly, Sentinel-2 albedo sheds light on multiple important implications related to agriculture, forestry, and urban fields. For example, it can be used to help detect forest phenology (Figs. 9b-c, 15a, and S13b; Alibakhshi et al. 2020; Berbet and Costa, 2003; Wang et al. 2018; Williamson et al. 2016), improve cropland management practices (Figs. 9a, 15b and S13a; Davin et al. 2014; Lobell et al. 2006; Miller et al. 2016; Singarayer et al. 2009), monitor grassland growth (Fig. 9d and S12d; Abraha et al. 2021; Sciusco et al. 2020; Wang and Davidson, 2007; Zheng et al. 2021), renew urban built-up infrastructure (Fig. 14), and infer snow events (Fig. 15b). Secondly, Sentinel-2 albedo further allows the monitoring of fine-scale biophysical or biogeochemical processes. For example, it can be used to infer forest dynamics by linking forest albedo with the structural and compositional properties of trees (e.g. leaf area, canopy height, forest age, and species composition; Alibakhshi et al. 2020; Bright et al. 2018; Hovi et al. 2019; Kuusinen et al. 2014, 2016). It can also be used to assess urbanization activities by relating surface albedo to urban metrics (e.g. impervious cover fraction, urban greenspace, population density, and urban heat island; Kaplan et al. 2016; Trlica et al. 2017). More importantly, because the spatial resolution of Sentinel-2 is finer than or equal to most tree-crown diameters (Bush et al. 2020; Wu et al. 2021), it also offers a promising way to monitor individual-tree albedo which can improve our understanding of the individual-to-ecosystem scaling mechanisms of albedo-related ecological processes. Thirdly, this approach can produce a unique high-resolution surface albedo dataset from 2017 onward, which could be used to constrain the parameterization of Earth System Models in simulating the surface energy budget (Bonan and Doney, 2018; Brovkin et al. 2021), assess the impacts of human activity on global warming (Wohlfahrt et al. 2021; Zeng et al. 2021), and improve the future projection of climate change (Li et al. 2016; Ouyang et al. 2022; Wang et al. 2016a). Such a dataset would also benefit the remote sensing community, for instance, in refining algorithm development to generate high-resolution satellite albedo (Li et al. 2018). Lastly, our integrated evaluation framework provides a novel multi-scale protocol for assessing the accuracy of high-resolution satellite albedo. The use of 3-D radiative transfer model simulation, in particular, can offer valuable benchmarks when fine-scale ground measurements are lacking. This evaluation framework is transferable and applicable to other satellite sensors (e.g. Gaofen-2 and PlanetScope; Houborg and McCabe, 2018; Vos et al. 2019) with equivalent or superior spatial resolution compared to Sentinel-2.

Despite the successful implementations of our algorithm development, evaluation, and application, there are still several limitations that might cause a degree of uncertainties about our results and should be solved in future efforts. Firstly, regarding algorithm development, our validation results reveal that Sentinel-2 albedo shows a larger uncertainty over snow cover relative to snow-free surfaces because of the relatively poor-quality snow BRDF data from MODIS. Therefore, an integration of the snow physical BRDF models (e.g. the asymptotic radiative transfer (ART) model; Jiao et al. 2019; Qu et al. 2014) with high-resolution satellite data (e.g. 3-m PlanetScope with daily revisit; Cannistra et al. 2021; Planet Team, 2021; Roy et al. 2017, 2021; Wu et al. 2021) could improve the accuracy of our approach in mapping albedo over snow surfaces (Stroeve et al. 2006; Wang et al. 2012). Moreover, the spatial resolution differences between MODIS BRDF training samples and Sentinel-2 reflectance might also lead to some uncertainties. Thus, the physical BRDF models or their associated kernel-driven functions accounting for fine-scale surface characteristics (e.g. 3-D building morphology and topography relief) are expected to provide more accurate and representative BRDF datasets. Secondly, regarding algorithm evaluation, the lack of ground reference at high-resolution footprints makes the pixel-scale albedo evaluation a difficult task. Thus, we suggested that more ground measurements with flux footprints strictly matching the Sentinel-2 spatial resolution to be conducted to provide more reliable albedo benchmarks. Integrating unmanned aerial vehicles (UAVs) with hyperspectral imaging technology could also generate valuable references for evaluating satellite albedo. Additionally, the area-weighted aggregation approach used in this study without accounting for surface heterogeneity might also create some uncertainties in the albedo comparison between Sentinel-2 and MODIS. The multi-scale aggregation strategy involving the 3-D physical radiative transfer process (Lin et al. 2018, 2021) is suggested to be developed for albedo comparisons across satellites. Lastly, cloud cover and shadow cause critical data discontinuity in surface albedo. Therefore, gap-filling approaches should be developed to fill data gaps when generating long-term, 10-m surface albedo products for large-scale analysis (e.g. albedo changes due to vegetation greening and urbanization; Guo et al. 2022; Li et al. 2016).

6. Conclusions

The accurate mapping and monitoring of fine-scale surface albedo are essential to quantify the biophysical processes of natural dynamics and anthropogenic activities. In this study, we proposed a direct estimation approach to advance our capability of estimating high-quality and high-resolution surface albedo from 10-m Sentinel-2 satellites. Our results demonstrate that Sentinel-2 can accurately capture surface albedo and agree well with the 3-D DART simulations, ground measurements, and MODIS satellite product at the site, regional, and global scales. The pilot study demonstrates the promise of integrating the proposed approach with Sentinel-2 to map large-scale surface albedo at a 10-m spatial resolution and capture fine-scale surface dynamics. This will enhance Sentinel-2 data science, facilitate high-resolution surface energy balance mapping, monitoring and modeling, and further contribute to global change research.

Declaration of Competing Interest

The authors declare that they have no known competing financial interests or personal relationships that could have appeared to influence the work reported in this paper.

Acknowledgement

This work was supported by the Open Fund of State Key Laboratory of Remote Sensing Science under Grant No. OFSLRSS202017 awarded to S.W. X. L. was supported by the Chinese National Natural Science Foundation Project (#41901290). C.B. was supported by The University of Hong Kong HKU-100 Scholar Fund and Seed Fund for Strategic Interdisciplinary Research Scheme. G.Y. was supported by the European Union's Horizon 2020 research and innovation program under the Marie Skłodowska-Curie Grant (#835541). The authors would like to thank Prof. Jean-Philippe Gastellu-Etchegorry for providing 3-D DART model. The Sentinel-2 data were publicly accessed through the Google Earth Engine (GEE) cloud-computing platform. The authors would like to thank the AmeriFlux, BSRN, EuroFlux, HiWATER, SURFRAD, and NEON teams for providing tower-mounted flux measurements to derive ground benchmarks.

Appendix A. Supplementary data

Supplementary data to this article can be found online at https://doi.org/10.1016/j.isprsjprs.2022.09.016.

References

Abraha, M., Chen, J.Q., Hamilton, S.K., Sciusco, P., Lei, C., Shirkey, G., Yuan, J., Robertson, G.P., 2021. Albedo-induced global warming impact of Conservation Reserve Program grasslands converted to annual and perennial bioenergy crops. Environ. Res. Lett. 16, 84059–84069.

Alibakhshi, S., Naimi, B., Hovi, A., Crowther, T.W., Rautiainen, M., 2020. Quantitative analysis of the links between forest structure and land surface albedo on a global scale. Remote Sens. Environ. 246, 11854–11866.
Baldinelli, G., Bonafoni, S., Anniballe, R., Presciutti, A., Gioli, B., Magliulo, V., 2015. Spaceborne detection of roof and impervious surface albedo: Potentialities and comparison with airborne thermography measurements. Sol. Energy 113, 281–294.
Baldinelli, G., Bonafoni, S., Rotili, A., 2017. Albedo Retrieval From Multispectral Landsat 8 Observation in Urban Environment: Algorithm Validation by in situ Measurements. IEEE J. Sel. Top. Appl. Earth Obs. Remote Sens. 10, 4504–4511.
Baldocchi, D., Falge, E., Gu, L., Olson, R., Hollinger, D., Running, S., Anthoni, P., Bernhofer, C., Davis, K., Evans, R., 2001. FLUXNET: A new tool to study the temporal and spatial variability of ecosystem–scale carbon dioxide, water vapor, and energy flux densities. Bull. Am. Meteorol. Soc. 82, 2415–2434.
Berbet, M.L., Costa, M.H., 2003. Climate change after tropical deforestation: seasonal variability of surface albedo and its effects on precipitation change. J. Clim. 1612, 2099–2104.
Bonafoni, S., Sekertekin, A., 2020. Albedo Retrieval from Sentinel-2 by New Narrow-to-Broadband Conversion Coefficients. IEEE Geosci. Remote Sens. Lett. 179, 1618–1622.
Bonan, G.B., Doney, S.C., 2018. Climate, ecosystems, and planetary futures: the challenge to predict life in earth system models. Science 359 (6375) eaam8328-8337.
Breon, F.M., Maignan, F., 2017. A BRDF–BPDF database for the analysis of Earth target reflectances. Earth Syst. Sci. Data 9, 31–45.
Bright, R.M., Eisner, S., Lund, M.T., Majasalmi, T., Myhre, G., Astrup, R., 2018. Inferring Surface Albedo Prediction Error Linked to Forest Structure at High Latitudes. J. Geophys. Res. Atmos. 123, 4910–4925.
Brovkin, V., Brook, E., Williams, J.W., Bathiany, S., Lenton, T.M., Barton, M., DeConto, R.M., Donges, J.F., Ganopolski, A., McManus, J., Praetorius, S., de Vernal, A., Abe-Ouchi, A., Cheng, H., Claussen, M., Crucifix, M., Gallopín, G., Iglesias, V., Kaufman, D.S., Kleinen, T., Lambert, F., van der Leeuw, S., Liddy, H., Loutre, M.-F., McGee, D., Rehfeld, K., Rhodes, R., Seddon, A.W.R., Trauth, M.H., Vanderveken, L., Yu, Z.C., 2021. Past abrupt changes, tipping points and cascading impacts in the Earth system. Nat. Geosci. 14, 550–558.
Bush, E.R., Mitchard, E.T.A., Silva, T.S.F., Dimoto, E., Dimbonda, P., Makaga, L., Abernethy, K., 2020. Monitoring Mega-Crown Leaf Turnover from Space. Remote Sens. 12, 429–446.
Cannistra, A.F., Shean, D.E., Cristea, N.C., 2021. High-resolution CubeSat imagery and machine learning for detailed snow-covered area. Remote Sens. Environ. 258, 112399–112414.
Cao, C., Lee, X., Muhlhausen, J., Bonneau, L., Xu, J., 2018. Measuring Landscape Albedo Using Unmanned Aerial Vehicles. Remote Sens. 10, 1812–1828.
Cescatti, A., Marcolla, B., Vannan, S.K.S., Pan, J.Y., Roman, M.O., Yang, X.Y., Ciais, P., Cook, R.B., Law, B.E., Matteucci, G., Migliavacca, M., Moors, E., Richardson, A.D., Seufert, G., Schaaf, C.B., 2012. Intercomparison of MODIS albedo retrievals and in situ measurements across the global FLUXNET network. Remote Sens. Environ. 121, 323–334.
Che, T., Li, X., Liu, S.M., Li, H.Y., Xu, Z.W., Tan, J.L., Zhang, Y., Ren, Z.G., Xiao, L., Deng, J., Jin, R., Ma, M.G., Wang, J., Yang, X.F., 2019. Integrated hydrometeorological, snow and frozen-ground observations in the alpine region of the Heihe River Basin, China. Earth Syst. Sci. Data 11, 1483–1499.
Chen, J.M., Liu, J., 2020. Evolution of evapotranspiration models using thermal and shortwave remote sensing data. Remote Sens. Environ. 237, 111594–111614.
Chu, H.S., Luo, X.Z., Ouyang, Z., Chan, W.S., Dengel, S., Biraud, S.C., Torn, M.S., Metzger, S., Kumar, J., Arain, M.A., Arkebauer, T.J., Baldocchi, D., Bernacchi, C., Billesbach, D., Black, T.A., Blanken, P.D., Bohrer, G., Bracho, R., Brown, S., Brunsell, N.A., Chen, J., Chen, X., Clark, K., Desai, A.R., Duman, T., Durden, D., Fares, S., Forbrich, I., Gamon, J.A., Gough, C.M., Griffis, T., Helbig, M., Hollinger, D., Humphreys, E., Ikawa, H., Iwata, H., Ju, Y., Knowles, J.F., Knox, S.H., Kobayashi, H., Kolb, T., Law, B., Lee, X., Litvak, M., Liu, H., Munger, J.W., Noormets, A., Novick, K., Oberbauer, S.F., Oechel, W., Oikawa, P., Papuga, S.A., Pendall, E., Prajapati, P., Prueger, J., Quinton, W.L., Richardson, A.D., Russell, E.S., Scott, R.L., Starr, G., Staebler, R., Stoy, P.C., Stuart-Haëntjens, E., Sonnentag, O., Sullivan, R.C., Suyker, A., Ueyama, M., Vargas, R., Wood, J.D., Zona, D., 2021. Representativeness of Eddy-Covariance flux footprints for areas surrounding AmeriFlux sites. Agric. For. Meteorol. 301–302, 108350–108375.
Clark, R.N., Swayze, G.A., Wise, R., Livo, E., Hoefen, T., Kokaly, R., Sutley, S.J., 2007. USGS Digital Spectral Library splib06a. U.S, Geological Survey, Digital Data Series, p. 231.
Csiszar, I., Gutman, G., 1999. Mapping global land surface albedo from NOAA AVHRR. J. Geophys. Res. Atmos. 104, 6215–6228.
Davin, E.L., Seneviratne, S.I., Ciais, P., Olioso, A., Wang, T., 2014. Preferential cooling of hot extremes from cropland albedo management. Proc. Natl. Acad. Sci. 111, 9757–9761.
Dickinson, R.E., 1983. Land Surface Processes and Climate—Surface Albedos and Energy Balance. Adv. Geophys. 25, 305–353.
Diner, D.J., Beckert, J.C., Reilly, T.H., Bruegge, C.J., Conel, J.E., Kahn, R.A., Martonchik, J.V., Ackerman, T.P., Davies, R., Gerstl, S.A.W., Gordon, H.R., Muller, J., Myneni, R.B., Sellers, P.J., Pinty, B., Verstraete, M.M., 1998. Multi-angle Imaging SpectroRadiometer (MISR) instrument description and experiment overview. IEEE Trans. Geosci. Remote Sens. 36 (4), 1072–1087.
Drusch, M., Del Bello, U., Carlier, S., Colin, O., Fernandez, V., Gascon, F., Hoersch, B., Isola, C., Laberinti, P., Martimort, P., 2012. Sentinel-2: ESA's optical high-resolution mission for GMES operational services. Remote Sens. Environ. 120, 25–36.
Dubayah, R., Blair, J.B., Goetz, S., Fatoyinbo, L., Hansen, M., Healey, S., Hofton, M., Hurtt, G., Kellner, J., Luthcke, S., Armston, J., Tang, H., Duncanson, L., Hancock, S., Jantz, P., Marselis, S., Patterson, P.L., Qi, W., Silva, C., 2020. The Global Ecosystem Dynamics Investigation: High-resolution laser ranging of the Earth's forests and topography. Sci. Remote Sens. 1, 100002–100016.
Franch, B., Vermote, E.F., Claverie, M., 2014. Intercomparison of Landsat albedo retrieval techniques and evaluation against in situ measurements across the US SURFRAD network. Remote Sens. Environ. 152, 627–637.
Franch, B., Vermote, E., Skakun, S., Roger, J.C., Santamaria-Artigas, A., Villaescusa-Nadal, J.L., Masek, J., 2018. Toward Landsat and Sentinel-2 BRDF Normalization and Albedo Estimation: A Case Study in the Peruvian Amazon Forest. Front. Earth Sci. 6, 185–190.
Gao, F., He, T., Masek, J.G., Shuai, Y., Schaaf, C.B., Wang, Z., 2014. Angular Effects and Correction for Medium Resolution Sensors to Support Crop Monitoring. IEEE J. Sel. Top. Appl. Earth Obs. Remote Sens. 7, 4480–4489.
Gastellu-Etchegorry, J.-P., Yin, T., Lauret, N., Cajgfinger, T., Gregoire, T., Grau, E., Feret, J.-B., Lopes, M., Guilleux, J., Dedieu, G., Malenovský, Z., Cook, B., Morton, D., Rubio, J., Durrieu, S., Cazanave, G., Martin, E., Ristorcelli, T., 2015. Discrete anisotropic radiative transfer (DART 5) for modeling airborne and satellite spectroradiometer and LIDAR acquisitions of natural and urban landscapes. Remote Sens. 7 (2), 1667–1701.
Guo, T., He, T., Liang, S., Roujean, J.L., Zhou, Y., Huang, X., 2022. Multi-decadal analysis of high-resolution albedo changes induced by urbanization over contrasted Chinese cities based on Landsat data. Remote Sens. Environ. 269, 112832–112851.
Hao, D., Wen, J., Xiao, Q., Wu, S., Lin, X., Dou, B., You, D., Tang, Y., 2018. Simulation and analysis of the topographic effects on snow-free albedo over rugged terrain. Remote Sens. 10 (2), 278–298.
He, T., Liang, S.L., Wang, D.D., Cao, Y.F., Gao, F., Yu, Y.Y., Feng, M., 2018. Evaluating land surface albedo estimation from Landsat MSS, TM, ETM plus, and OLI data based on the unified direct estimation approach. Remote Sens. Environ. 204, 181–196.
Hemmerling, J., Pflugmacher, D., Hostert, P., 2021. Mapping temperate forest tree species using dense Sentinel-2 time series. Remote Sens. Environ. 267, 112743–112756.
Houborg, R., McCabe, M.F., 2018. A cubesat enabled spatio-temporal enhancement method (cestem) utilizing planet, Landsat and MODIS data. Remote Sens. Environ. 209, 211–226.
Hovi, A., Lindberg, E., Lang, M., Arumae, T., Peuhkurinen, J., Sirparanta, S., Pyankov, S., Rautiainen, M., 2019. Seasonal dynamics of albedo across European boreal forests: Analysis of MODIS albedo and structural metrics from airborne LiDAR. Remote Sens. Environ. 224, 365–381.
Hu, Z., Islam, S., Jiang, L.E., 1999. Approaches for aggregating heterogeneous surface parameters and fluxes for mesoscale and climate models. Bound.-Layer Meteorol. 93, 313–336.
Jiao, Z., Ding, A., Kokhanovsky, A., Schaaf, C., Bréon, F.M., Dong, Y., Wang, Z., Liu, Y., Zhang, X., Yin, S., Cui, L., Mei, L., Chang, Y., 2019. Development of a snow kernel to better model the anisotropic reflectance of pure snow in a kernel-driven BRDF model framework. Remote Sens. Environ. 221, 198–209.
Kaplan, S., Galletti, C.S., Chow, W.T.L., Myint, S.W., 2016. First order approximation of Broadband Directional Albedo with High Resolution Quickbird Imagery: a case study for arid urban areas. GIScience Remote Sens. 53, 303–319.
Kuusinen, N., Tomppo, E., Shuai, Y., Berninger, F., 2014. Effects of forest age on albedo in boreal forests estimated from MODIS and Landsat albedo retrievals. Remote Sens. Environ. 145, 145–153.
Kuusinen, N., Stenberg, P., Korhonen, L., Rautiainen, M., Tomppo, E., 2016. Structural factors driving boreal forest albedo in Finland. Remote Sens. Environ. 175, 43–51.
Levy, C.R., Burakowski, E., Richardson, A.D., 2018. Novel Measurements of Fine-Scale Albedo: Using a Commercial Quadcopter to Measure Radiation Fluxes. Remote Sens. 10, 1303–1317.
Li, Z., Erb, A., Sun, Q.S., Liu, Y., Shuai, Y.M., Wang, Z.S., Boucher, P., Schaaf, C., 2018. Preliminary assessment of 20-m surface albedo retrievals from sentinel-2A surface reflectance and MODIS/VIIRS surface anisotropy measures. Remote Sens. Environ. 217, 352–365.
Li, W., Fang, H., 2015. Estimation of direct, diffuse, and total FPARs from Landsat surface reflectance data and ground-based estimates over six FLUXNET sites. J. Geophys. Res. Biogeosci. 120, 96–112.
Li, Y., Wang, T., Zeng, Z., Peng, S., Lian, X., Piao, S., 2016. Evaluating biases in simulated land surface albedo from CMIP5 global climate models. J. Geophys. Res. Atmos. 121 (11), 6178–6190.
Liang, S.L., 2004. Quantitative Remote Sensing of Land Surfaces. Wiley, New York, USA.
Liang, S.L., Strahler, A.H., Walthall, C., 1999. Retrieval of land surface albedo from satellite observations: A simulation study. J. Appl. Meteorol. 38, 712–725.
Liang, S.L., Shuey, C.J., Russ, A.L., Fang, H., Chen, M., Walthall, C.L., Daughtry, C.S.T., Hunt, R., 2002. Narrowband to broadband conversions of land surface albedo: II. Validation. Remote Sens. Environ. 84, 25–41.
Liang, S.L., Zhao, X., Liu, S.H., Yuan, W.P., Cheng, X., Xiao, Z.Q., Zhang, X.T., Liu, Q., Cheng, J., Tang, H.R., Qu, Y.H., Bo, Y.C., Qu, Y., Ren, H.Z., Yu, K., Townshend, J., 2013. A long-term Global LAnd Surface Satellite GLASS dataset for environmental studies. Int. J. Digit. Earth 6, 5–33.
Liang, S.L., Wang, D.D., He, T., Yu, Y.Y., 2019. Remote sensing of earth's energy budget: synthesis and review. Int. J. Digit. Earth 12, 737–780.
Lin, X.W., Wen, J.G., Liu, Q.H., Xiao, Q., You, D.Q., Wu, S.B., Hao, D.L., Wu, X.D., 2018. A Multi-Scale Validation Strategy for Albedo Products over Rugged Terrain and Preliminary Application in Heihe River Basin, China. Remote Sens. 10, 156–174.
Lin, X.W., Wu, S.B., Hao, D.L., Wen, J.G., Liu, Q., H., 2021. Sloping Surface Reflectance: The Best Option for Satellite-Based Albedo Retrieval Over Mountainous Areas. IEEE Geosci. Remote Sens. Lett., 19, pp. 1–5.
Liu, Y., Wang, Z.S., Sun, Q., Erb, A.M., Li, Z., Schaaf, C.B., Zhang, X., Roman, M.O., Scott, R.L., Zhang, Q., Novick, K.A., Bret-Harte, M.S., Petroy, S., SanClements, M.,

2017. Evaluation of the VIIRS BRDF, Albedo and NBAR products suite and an assessment of continuity with the long term MODIS record. Remote Sens. Environ. 201, 256–274.
Lobell, D.B., Bala, G., Duffy, P.B., 2006. Biogeophysical impacts of cropland management changes on climate. Geophys. Res. Lett. 33, L06708–6712.
Lucht, W., Schaaf, C.B., Strahler, A.H., 2000. An algorithm for the retrieval of albedo from space using semi-empirical BRDF models. IEEE Trans. Geosci. Remote Sens. 38, 977–998.
Ma, Y., He, T., Liang, S., Wen, J., Gastellu-Etchegorry, J.P., Chen, J., Ding, A., Feng, S., 2022. Landsat snow-free surface albedo estimation over sloping terrain: Algorithm development and evaluation. IEEE Trans. Geosci. Remote Sens. 60, 440891–440905.
Marshall, M., Aneece, I., Foley, D., Xueliang, C., Biggs, T., 2018. Crop Water Productivity Estimation with Hyperspectral Remote Sensing. *In Advanced Applications in Remote Sensing of Agricultural Crops and Natural Vegetation*. CRC Press, pp. 79–96.
Mihailovic, D.T., Kapor, D., Cirisan, A., Firanj, A., 2012. Parameterization of the albedo over the heterogeneous surfaces for different geometries in a land surface scheme by the Monte Carlo Ray-tracing method. Atmos. Res. 107, 51–68.
Miller, J., Beasley, B., Drury, C., Larney, F., Hao, X., Chanasyk, D., 2016. Influence of long-term application of feedlot amendments to cropland on ground elevation, Ah horizon depth, and soil color. Can. J. Soil Sci. 97, 109–121.
Ouyang, Z., Sciusco, P., Jiao, T., Feron, S., Lei, C., Li, F., Chen, J., 2022. Albedo changes caused by future urbanization contribute to global warming. Nat. Commun. 13 (1), 1–9.
Planet Team, Planet Imagery Product Specifications February 2021, Available online: https://www.planet.com/products/ (2021) (last accessed on August 5, 2021).
Potter, S., Solvik, K., Erb, A., Goetz, S.J., Johnstone, J.F., Mack, M.C., Randerson, J.T., Roman, M.O., Schaaf, C.L., Turetsky, M.R., Veraverbeke, S., Walker, X.J., Wang, Z., Massey, R., Rogers, B.M., 2020. Climate change decreases the cooling effect from postfire albedo in boreal North America. Glob. Change Biol. 26, 1592–1607.
Qu, Y., Liu, Q., Liang, S.L., Wang, L.Z., Liu, N.F., Liu, S.H., 2014. Direct-Estimation Algorithm for Mapping Daily Land-Surface Broadband Albedo From MODIS Data. IEEE Trans. Geosci. Remote Sens. 52, 907–919.
Rojas-Robles, N.E., Garatuza-Payán, J., Álvarez-Yépiz, J.C., Sánchez-Mejía, Z.M., Vargas, R., Yépez, E.A., 2020. Environmental controls on carbon and water fluxes in an old-growth tropical dry forest. J. Geophys. Res.-Biogeosci. 125.
Román, M.O., Gatebe, C.K., Shuai, Y., Wang, Z., Gao, F., Masek, J.G., He, T., Liang, S., Schaaf, C.B., 2013. Use of In Situ and Airborne Multiangle Data to Assess MODIS- and Landsat-Based Estimates of Directional Reflectance and Albedo. IEEE Trans. Geosci. Remote Sens. 51, 1393–1404.
Roy, D.P., Li, J., Zhang, H.K.K., Yan, L., Huang, H.Y., Li, Z.B., 2017. Examination of Sentinel 2A multi-spectral instrument MSI reflectance anisotropy and the suitability of a general method to normalize MSI reflectance to nadir BRDF adjusted reflectance. Remote Sens. Environ. 199, 25–38.
Roy, D.P., Huang, H., Houborg, R., Martins, V.S., 2021. A global analysis of the temporal availability of PlanetScope high spatial resolution multi-spectral imagery. Remote Sens. Environ. 264, 112586–112611.
Schaaf, C.B., Gao, F., Strahler, A.H., Lucht, W., Li, X., Tsang, T., Strugnell, N.C., Zhang, X., Jin, Y., Muller, J.-P., Lewis, P., Barnsley, M., Hobson, P., Disney, M., Roberts, G., Dunderdale, M., Doll, C., d'Entremont, R.P., Hu, B., Liang, S., Privette, J. L., Roy, D., 2002. First operational BRDF, albedo nadir reflectance products from MODIS. Remote Sens. Environ. 83, 135–148.
Schwerdtfeger, P., 2002. Interpretation of airborne observations of the albedo. Environ. Model. Softw. 17, 51–60.
Sciusco, P., Chen, J., Abraha, M., Lei, C., Robertson, G.P., Lafortezza, R., Shirkey, G., Ouyang, Z., Zhang, R., John, R., 2020. Spatiotemporal variations of albedo in managed agricultural landscapes: inferences to global warming impacts GWI. Landscape Ecol. 35, 1385–1402.
Sentinel-2 Team, 2021. SENTINEL-2 user handbook July 2021, Available online: https://earth.esa.int/documents/247904/685211/Sentinel-2_User_Handbook/ (2021) (last accessed on August 5, 2021).
Shuai, Y.M., Masek, J.G., Gao, F., Schaaf, C.B., 2011. An algorithm for the retrieval of 30-m snow-free albedo from Landsat surface reflectance and MODIS BRDF. Remote Sens. Environ. 115, 2204–2216.
Shuai, Y.M., Masek, J.G., Gao, F., Schaaf, C.B., He, T., 2014. An approach for the long-term 30-m land surface snow-free albedo retrieval from historic Landsat surface reflectance and MODIS-based a priori anisotropy knowledge. Remote Sens. Environ. 152, 467–479.
Singarayer, J.S., Ridgwell, A., Irvine, P., 2009. Assessing the benefits of crop albedo bio-geoengineering. Environ. Res. Lett. 4, 045110–045118.
Stroeve, J.C., Box, J.E., Haran, T., 2006. Evaluation of the MODIS (MOD10A1) daily snow albedo product over the Greenland ice sheet. Remote Sens. Environ. 105 (2), 155–171.
Trlica, A., Hutyra, L.R., Schaaf, C.L., Erb, A., Wang, J.A., 2017. Albedo, Land Cover, and Daytime Surface Temperature Variation Across an Urbanized Landscape. Earth's Future 5, 1084–1101.
Vanderhoof, M., Williams, C.A., Shuai, Y., Jarvis, D., Kulakowski, D., Masek, J., 2014. Albedo-induced radiative forcing from mountain pine beetle outbreaks in forests, south-central Rocky Mountains: magnitude, persistence, and relation to outbreak severity. Biogeosci. 11, 563–575.
Vos, K., Harley, M.D., Splinter, K.D., Simmons, J.A., Turner, I.L., 2019. Sub-annual to multi-decadal shoreline variability from publicly available satellite imagery. Coast. Eng. 150, 160–174.
Wang, L.B., Cole, J.N., Bartlett, P., Verseghy, D., Derksen, C., Brown, R., von Salzen, K., 2016a. Investigating the spread in surface albedo for snow-covered forests in CMIP5 models. J. Geophys. Res. Atmos. 121 (3), 1104–1119.
Wang, S.S., Davidson, A., 2007. Impact of climate variations on surface albedo of a temperate grassland. Agric. For. Meteorol. 142, 133–142.
Wang, Z., Erb, A.M., Schaaf, C.B., Sun, Q., Liu, Y., Yang, Y., Shuai, Y., Casey, K.A., Roman, M.O., 2016b. Early spring post-fire snow albedo dynamics in high latitude boreal forests using Landsat-8 OLI data. Remote Sens. Environ. 185, 71–83.
Wang, D.D., Liang, S.L., He, T., Yu, Y.Y., 2013. Direct estimation of land surface albedo from VIIRS data: Algorithm improvement and preliminary validation. J. Geophys. Res. Atmos. 118 (22), 12577–12586.
Wang, D.D., Liang, S.L., He, T., Yu, Y.Y., Schaaf, C., Wang, Z.S., 2015. Estimating daily mean land surface albedo from MODIS data. J. Geophys. Res. Atmos. 120, 4825–4841.
Wang, Z.S., Schaaf, C.B., Chopping, M.J., Strahler, A.H., Wang, J.D., Roman, M.O., Rocha, A.V., Woodcock, C.E., Shuai, Y.M., 2012. Evaluation of Moderate-resolution Imaging Spectroradiometer MODIS snow albedo product MCD43A over tundra. Remote Sens. Environ. 117, 264–280.
Wang, Z.S., Schaaf, C.B., Sun, Q.S., Shuai, Y.M., Roman, M.O., 2018. Capturing rapid land surface dynamics with Collection V006 MODIS BRDF/NBAR/Albedo MCD43 products. Remote Sens. Environ. 207, 50–64.
Wang, J.D., Zhang, L.X., Liu, Q.H., Zhang, B., Yin, Q., 2009. Spectral Library of Typical Objects in China. Science Press, Beijing, Beijing.
Wen, J., Liu, Q., Xiao, Q., Liu, Q., You, D., Hao, D., Wu, S., Lin, X., 2018. Characterizing land surface anisotropic reflectance over rugged terrain: A review of concepts and recent developments. Remote Sens. 10 (3), 370–400.
Wen, J., You, D., Han, Y., Lin, X., Wu, S., Tang, Y., Liu, Q., 2022. Estimating Surface BRDF/Albedo over Rugged Terrain Using an Extended Multi-Sensor Combined BRDF Inversion (EMCBI) Model. IEEE Geosci. Remote Sens. Lett. 19, 1–5.
Williamson, S.N., Barrio, I.C., Hik, D.S., Gamon, J.A., 2016. Phenology and species determine growing-season albedo increase at the altitudinal limit of shrub growth in the sub-Arctic. Glob. Change Biol. 2211, 3621–3631.
Wohlfahrt, G., Tomelleri, E., Hammerle, A., 2021. The albedo–climate penalty of hydropower reservoirs. Nat. Energy 6, 372–377.
Wu, S.B., Wen, J.G., You, D.Q., Hao, D.L., Lin, X.W., Xiao, Q., Liu, Q.H., Gastellu-Etchegorry, J.P., 2018. Characterization of Remote sensing Albedo Over Sloped Surfaces Based on DART Simulations and In Situ Observations. J. Geophys. Res. Atmos. 123, 8599–8622.
Wu, S.B., Wen, J.G., Gastellu-Etchegorry, J.P., Liu, Q.H., You, D.Q., Xiao, Q., Hao, D.L., Lin, X.W., Yin, T.G., 2019. The definition of remotely sensed reflectance quantities suitable for rugged terrain. Remote Sens. Environ. 225, 403–415.
Wu, S.B., Wang, J., Yan, Z., Song, G., Chen, Y., Ma, Q., Deng, M., Wu, Y., Zhao, Y., Guo, Z., Yuan, Z., Dai, G., Xu, X., Yang, X., Su, Y., Liu, L., Wu, J., 2021. Monitoring tree-crown scale autumn leaf phenology in a temperate forest with an integration of PlanetScope and drone remote sensing observations. ISPRS J. Photogramm. Remote Sens. 171, 36–48.
Wu, X.D., Wen, J.G., Xiao, Q., Liu, Q., Peng, J.J., Dou, B.C., Li, X.H., You, D.Q., Tang, Y., Liu, Q.H., 2016. Coarse scale in situ albedo observations over heterogeneous snow-free land surfaces and validation strategy: A case of MODIS albedo products preliminary validation over northern China. Remote Sens. Environ. 184, 25–39.
Wu, X.D., Wen, J.G., Xiao, Q., Yu, Y.Y., You, D.Q., Hueni, A., 2017. Assessment of NPP VIIRS albedo over heterogeneous crop land in Northern China. J. Geophys. Res. Atmos. 122, 13138–13154.
Zeng, Z., Wang, D., Yang, L., Wu, J., Ziegler, A.D., Liu, M., Ciais, P., Searchinger, T.D., Yang, Z.-L., Chen, D., 2021. Deforestation-induced warming over tropical mountain regions regulated by elevation. Nat. Geosci. 14, 23–29.
Zhang, Q., Barnes, M., Benson, M., Burakowski, E., Oishi, A.C., Ouimette, A., Sanders-DeMott, R., Stoy, P.C., Wenzel, M., Xiong, L., Yi, K., Novick, K.A., 2020a. Reforestation and surface cooling in temperate zones: Mechanisms and implications. Glob. Change Biol. 26, 3384–3401.
Zhang, X.N., Jiao, Z.T., Dong, Y.D., He, T., Ding, A.X., Yin, S.Y., Zhang, H., Cui, L., Chang, Y.X., Guo, J., Xie, R., 2020b. Development of the Direct-Estimation Albedo Algorithm for Snow-Free Landsat TM Albedo Retrievals Using Field Flux Measurements. IEEE Trans. Geosci. Remote Sens. 58, 1550–1567.
Zheng, L., Qi, Y., Qin, Z., Xu, X., Dong, J., 2021. Assessing albedo dynamics and its environmental controls of grasslands over the Tibetan Plateau. Agric. For. Meteorol. 307, 108479–108490.
Zhong, S.Y., Xiao, Q., Wen, J.G., Zheng, X.M., Ma, M.G., Qu, Y., Zheng, K., Chi, T.H., Tang, Y., You, D.Q., 2020. Design and realization of ground object background spectral library for surveying and mapping. J. Remote Sens. 24, 701–716.
Zhou, Y., Wang, D., Liang, S., Yu, Y., He, T., 2016. Assessment of the Suomi NPP VIIRS land surface albedo data using station measurements and high-resolution albedo maps. Remote Sens. 8 (2), 137–153.